

MODELLING, DESIGN OPTIMIZATION AND CONTROL OF MAGNETO
RHEOLOGICAL BRAKES FOR AUTOMOTIVE APPLICATIONS

Hadi Shamieh

A Thesis

in the

Department of

Mechanical and Industrial Engineering

Presented in Partial Fulfillment of the Requirements

For the Degree of Master of Applied Science at

Concordia University

Montreal, Quebec, Canada

January 2017

©Hadi Shamieh, 2017

CONCORDIA UNIVERSITY

School of Graduate Studies

This is to certify that the thesis prepared

By: Hadi Shamieh

Entitled: Modelling, Design Optimization and Control of Magneto Rheological Brakes for Automotive Applications

and submitted in partial fulfillment of the requirements for the degree of

Master of Applied Science (Mechanical Engineering)

complies with the regulations of the University and meets the accepted standards with respect to originality and quality.

Signed by the final examining committee:

Dr. Gerard Gouw, MIE Chair

Dr. Ion Stiharu, MIE Examiner

Dr. Khaled Galal, BCEE Examiner (External)
External Member

Dr. Ramin Sedaghati, MIE Supervisor

Approved by _____
Dr. S. Narayanswamy, M.A.Sc. Program Director
Department of Mechanical and Industrial Engineering

Dr. A. Asif, Dean
Faculty of Engineering & Computer Science

Date January 12, 2017

ABSTRACT

Modelling, Design Optimization and Control of Magneto Rheological Brakes for Automotive Applications

Hadi Shamieh

The braking system is one of the major factors affecting a vehicle's performance. The future of the automotive industry thrives by the creation of a greener, more efficient and lightweight braking mechanisms. Research on utilizing electromechanical brakes have shown potential due to their superior performance and controllability. The magnetorheological Brake (MRB) is a promising electromechanical brake which can provide variable damping through variation of the MR fluids' apparent viscosity and yield strength using the applied magnetic field. Fast response time, low power requirement and large dynamic range are among unique features of MRBs making them an ideal candidate for vehicle applications. While some design configurations have been proposed for applying MRBs in the automotive industry, the commercial application has not yet been fully realized mainly due to the existence of their zero-field viscous torque. The focal purpose of this study is to propose and develop a novel real-size vehicle model of the MRB design with absolutely no energy loss in terms of viscous torque generation. The design is achieved using permanent magnets which force the MR fluid volume to shift locations between the brake's operating modes – 'on' and 'off' – to allow complete de-coupling. The performance of the proposed design compared with the conventional design is demonstrated on a 2-disk-type MRB configuration. The Herschel-Bulkley constitutive model is adopted for the MR fluid to derive the mathematical equations governing the systems' braking torques as a function of the rotational speed, geometric properties, and applied electrical current. The MR fluid selected for the proposed designs is MRF-132DG from Lord Corporation. Analytical magnetic circuit analysis of the MRB design has been conducted which allows to approximately derive the relation between the magnetic field intensity and the electric current as a function of number of coil turns and the brake's geometric variables. The analytical model is then verified using an electromagnetic finite element model developed in open source FEMM software. An equation relating densities of the materials used in the MRB and their corresponding dimensions is also derived to estimate the weight of the proposed MRB. Subsequently, a multidisciplinary design optimization problem has been formulated to identify the

optimal brake geometrical parameters to maximize the dynamic range of the MRBs under weight, size and magnetic flux density constraints. The optimization problem has been solved using Genetic Algorithm (GA) followed by the Sequential Quadratic Programming (SQP) technique implemented in the MATLAB environment to achieve the true global optimal design. It is shown that the proposed MRB design provides better performance specifications under the required design constraints while having zero viscous torque generation making it suitable for application in real commercial vehicles. Finally, a simple dynamic quarter-vehicle model integrated with the optimally designed MRB has been considered to investigate the brake performance in automotive application. A PID control scheme has been designed for optimal wheel slip control over different road surface conditions. The objective is to obtain the highest value possible for the road-friction coefficient. This is possible through regulating and maintaining the slip ratio to a desired value whether driving on dry, wet, snowy or icy roads. The controller is purposed to enhance the overall braking properties of a vehicle through reducing the stopping distance and time, enhancing stability, and avoiding wheel lockup.

ACKNOWLEDGEMENTS

The individual merely responsible for the successful completion of this research is Professor Ramin Sedaghati. Not only am I thankful for his generous supervision and exceptional guidance through the research, but also I would like to especially thank Professor Sedaghati for his trust and believe in me even before he had met me. Professor Ramin was continually available for meeting and discussing new ideas. He has relentlessly provided me with helpful tips to promote my work and results.

Furthermore, the effective completion would not have been possible without the support of certain close friends and family members who kept me motivated along the way. I am grateful for the trust and support of my parents and siblings throughout my education. A distinct acknowledgment must be given to my best friend and partner in crime, Rula Dahdal, for she was the main motive behind my strong determination for efficiency and perfection in my research.

Finally, I would like to express my gratitude towards my fellow colleagues and faculty members in the Mechanical and Industrial Engineering department at Concordia University. I am thankful to be part of a strong resourceful community that I can easily reach out to when in need of guidance.

TABLE OF CONTENTS

List of Figures	ix
List of Tables	xii
Chapter 1 Literature Review	1
1.1. Introduction:	1
1.2. MR Fluids, their Applications and Operational Modes:	2
1.3. The Magneto-Rheological Brake:	4
1.4. Review of Relevant Literature:	6
1.5. Overall Scope of the Research:	11
1.6. Organization of the Dissertation:	11
Chapter 2 Magneto-Rheological Brake-Damping Torque Formulation	13
2.1. Introduction:	13
2.2. Derivation of the Braking Torque – Conventional MRB:	13
2.3. Torque equations based on the Bingham Plastic Model:	17
2.4. MR Fluid Field-Dependent Yield Stress:	18
2.5. Torque Equations based on the Herschel-Bulkley model:	19
2.6. Torque Equations for a Multiple Disk MRB:	24
2.7. Novel Decoupled Design:	25
2.8. Summary:	29
Chapter 3 MR BRAKE Magnetic Circuit and Temperature Analysis	30

3.1. Introduction:	30
3.2. Preliminary Design:.....	30
3.3. Analytical Magnetostatic Circuit Analysis - Conventional MRB:.....	31
3.4. Finite Element Analysis of the MRB Magnetic Circuit:	36
3.5. Analytical Magneto-static Circuit Analysis - The decoupled MRB design:.....	38
3.6. Temperature Build-Up-Heat Dissipation:	42
3.7. Summary:	47
Chapter 4 Design Optimization of the MRB	48
4.1. Introduction:	48
4.2. The Performance Indices:.....	48
4.3. Multi-Disciplinary Optimization Problem:	51
4.3.1. The Conventional MRB Design.....	51
4.3.2. The Novel Decoupled MRB Design.....	52
4.4. Multi-Objective Optimization Results:	54
4.5. Additional investigation on weighting factors distribution:.....	59
4.7. CAD Model of the Optimal Proposed Design:	66
4.8. Summary:	66
Chapter 5 Application of MRB in Real-Size vehicle.....	68
5.1. Introduction:	68
5.2. Vehicle Dynamic Model:	68

5.3. MRB Control:.....	71
5.3.1. MRB-Vehicle Plant:.....	71
5.3.2. PID Configurations:.....	74
4.3.3. PID Controller Design:.....	75
5.4. Simulation Results:.....	79
5.4.1. Effect of the Time Constant block:.....	79
5.4.2. Simulation results on different road conditions:.....	80
5.4.3. Open-loop response of the MRB-Vehicle plant:.....	83
5.4.4. Antilock-Braking-System of the conventional hydraulic brake:.....	85
5.5. Summary:.....	86
Chapter 6 Conclusions.....	87
6.1. Introduction:.....	87
6.2. Major Contributions:.....	88
6.3. Explanation of Limitations:.....	88
6.4. Recommendations for Future Works:.....	89
References.....	91
Appendix A: MRB Weight Estimation Equation.....	94
A.1. The conventional MRB Design:.....	94
A.2. Novel MRB Design:.....	95
Appendix B: CATIA Drawing of the novel MRB.....	96

LIST OF FIGURES

Figure 1.1 - A schematic description of the MR fluid working modes, (a) Flow mode, (b) Shear mode, (c) Squeeze mode, (d) Pinch mode	3
Figure 1.2 - Different types of MRB: (a) drum, (b) inverted drum, (c) T-shaped rotor, (d) disk, and (e) multiple disks [4]......	5
Figure 1.3 – Gravity based MRB design in (a) off state and (b) on state.	8
Figure 1.4 – MRB design based on centrifugal forces in (a) off and (b) on states.	9
Figure 1.5 – MRB design with PM in (a) off and (b) on states.	10
Figure 2.1 – Sectioned dimensioning of the MRB.	14
Figure 2.2 – Shear stress as a function of Shear rate for MRF-132DG at 0A.	16
Figure 2.3 – Yield Stress versus Magnetic Field Strength for MR-132DG [18]......	19
Figure 2.4 – Comparison of Shear stress versus Shear rate for MRF-132DG at 0A.....	21
Figure 2.5 – Shear stress vs. Shear rate at different magnetic flux densities.....	21
Figure 2.6 – Magnetic field Density versus Intensity for MRF-132DG.....	22
Figure 2.7 – Proposed Decoupled Design.....	26
Figure 2.8 – Novel de-coupling design in (a) off-state and (b) on state.	27
Figure 3.1 – The Magnetic Circuit of the MRB.....	33
Figure 3.2 - Area box for the MRB wires.	35
Figure 3.3 - Distribution of the magnetic flux density in the conventional MRB design using the FEMM software.	37

Figure 3.4 - The variation of flux density over the length of the MR fluid gap.	37
Figure 3.5 - Section sketch of the shear gap region the proposed MRB design in (a) OFF and (b) ON modes.	40
Figure 3.6 - FBD of MR fluid situated on (a) top end and (b) bottom end of the MRB.	41
Figure 3.7 - Temperature distribution of the conventional MRB – Kinetic energy conversion. ...	43
Figure 3.8 - Temperature distribution of the conventional MRB due to the shear stresses.	46
Figure 4.1 - Electric Current vs. Time Constant.	50
Figure 4.2 - Change of objective function as a function of weighting factor.	60
Figure 4.3 - Zoomed resolution of the objective function value over the weighting interval.	61
Figure 4.4 - MRB performance specs versus maximum torque weighting factor.	62
Figure 4.5 - TC versus T_b for the different design points.	63
Figure 4.6 - Addition of R_{es} to the car battery – MRB electric circuit.	64
Figure 4.7 - Variation of PC versus TC for different R_{es}	65
Figure 4.8 – CAD model of the optimal configuration of the proposed MRB.	66
Figure 5.1 - Vehicle Wheel – Free body diagram.	68
Figure 5.2 - Friction Coefficient as a function of different road surfaces [32].	70
Figure 5.3 - SIMULINK model of MRB-vehicle plant.	72
Figure 5.4 - PID Controller configurations: (a) Open loop, (b) textbook PID, (c) derivative-of- output, and (d) set-point-on-I controller.	74
Figure 5.5 - PID Controller connection to the MRB Vehicle Plant.	75

Figure 5.6 - Slip ratio with PID controller for varied proportional gains, k_p , $k_I=k_D=0$	77
Figure 5.7 - Slip ratio with the PID controller for varied integral gains, k_I , $k_p=29$ and $k_D=0$	78
Figure 5.8 - Slip ratio with the PID controller for varied proportional gains, k_D , $k_p=29$ and $k_I=-0.1$	79
Figure 5.9 - Simulation Results with and without TC response.	80
Figure 5.10 - Simulation results for wet roads.....	81
Figure 5.11 - Simulation results for a snowy road.....	81
Figure 5.12 - Simulation results for an icy road.	82
Figure 5.13 - Open loop system responses due to constant current inputs-Icy Road.	84
Figure 5.14 - Wheel speed of a hydraulic brake with ABS for different road conditions.	85

LIST OF TABLES

Table 1.1 - Previous design achievements for the Automotive MRB.	7
Table 3.1 - Geometric variables for the preliminary design of the MRB.	30
Table 3.2 - Properties required to calculate the thermal effusivity.....	44
Table 4.1 - Design variables and their ranges for the conventional MRB design.	52
Table 4.2 – New additional design variables and their ranges for the proposed MRB design.	54
Table 4.3 - Genetic Algorithm Results – Design Parameters.	55
Table 4.4 - Genetic Algorithm Results – MRB Characteristics.....	56
Table 4.5 - True and Absolute Global Optimization Results using combined GA and SQP.	58
Table 4.6 - Geometric variables and specifications for the selected optimal MRB design.	65
Table 5.1 - Parameters for the quarter car model with MRB.....	71

CHAPTER 1

LITERATURE REVIEW

1.1. Introduction:

The automotive industry has a constant requisite of developing innovative methods to raise the standards of transportation vehicles to meet the requests and desires of its clients. Automotive engineers are committed to modernizing today's vehicles through increasing its performance capabilities, decreasing the environmental impacts and reducing vehicle weight and production cost. One vital method that developed in the past few decades that focuses on all these modernizing constraints is the consideration of electromechanical systems. Research on implementing electromechanical systems in the automotive industry has been given specific attention by researchers around the world. Such systems allow better vehicle control through fast and direct electric actuation with real-time sensors rather than having to deal with traditional mechanical components like springs and brake pads. Smart devices with MR fluids offer a remarkable potential in the electro-mechanical interface. Some applications of these devices are dampers, valves, clutches and brakes [1].

The focus of this research is advancing the vehicle braking system through the modelling, optimization and control of an MR Brake. Primarily, it is essential to present the disadvantages of conventional brakes used in vehicles today. Due to the brakes mechanism working principle, the friction and localized heating wear out the brake disc. The particles resulting from this wear along with the brake pad dust are reported to have a significant contribution of environment pollution [2]. Another disadvantage of conventional brakes is that they frequently require pad replacement and disc surface refining [3]. Moreover, the response time of conventional brake is relatively slow.

The replacement of conventional brake by MRBs in the automotive vehicle eliminates all these disadvantages and even serves more benefits - to be discussed later in the literature review.

1.2. MR Fluids, their Applications and Operational Modes:

MR fluid is composed of a viscous fluid like water or oil which hosts small (micron-size) metallic particles. When a magnetic field is added, the iron particles (typically carbonyl iron powder due to its high magnetic saturation) line up upon the lines of the magnetic field (instead of sliding passed each other); thus, increasing the fluid's apparent viscosity and yield strength. LORD Corporation (<http://www.lordmrstore.com/>), is one of the top manufacturers of MR fluid, and provide different types of standard MR fluid made up of 20 to 40 percent by volume of relatively pure, 3 to 10-micron diameter iron particles. These particles are hosted by a viscous liquid such as mineral oil, synthetic oil, water or glycol. The maximum yield strengths for MR fluids (with iron particles) are 50 to 100 *kPa* for applied magnetic fields of 150 to 250 *kA/m*.

MR fluid is being studied for a wide variety of applications. MR dampers are of the most common applications of MR fluid. Recently, automotive companies utilized MR dampers as a vital part of their smart vehicle suspension systems for a smooth and safe ride. The US military uses MR dampers in the cockpit seats of their helicopters and their off-road Humvees. The US Military is also investing research to use MR fluids to enhance their body armors. Other applications are related to structural engineering where MR fluid dampers can be used to isolate shock and vibration in wider range of frequencies. Furthermore, MR fluid is being used to produce prosthetic limbs. They prevent injuries by simulating natural shock absorbers in the human joints. A modern application of MR fluid devices is the MR brake.

Despite the variety of its applications, the working principle of MR devices falls in one of four categories [4], displayed in Fig. 1.1. The first is the “flow mode” in which the fluid flow is parallel to the fixed contact surfaces and perpendicular to the direction of applied magnetic field as shown in Fig. 1.1(a). The “shear mode” is characterized by having one of the contact walls move with a given velocity in the direction of the wall and perpendicular to the applied magnetic field as seen in Fig. 1.1(b). The “squeeze mode” is similar to the shear mode except that the direction of velocity of the moving wall is perpendicular to the wall and parallel to the direction of the applied magnetic field as demonstrated in Figure 1.1(c). Finally, the “pinch mode” shown in Figure 1.1(d) is a version of the “flow mode” in which the magnetic field is applied in the direction of the fluid flow. In this mode, the magnetic flux distribution is non-linear, and the only activated part of the MR fluid is the one close to the separating non-magnetic spacer.

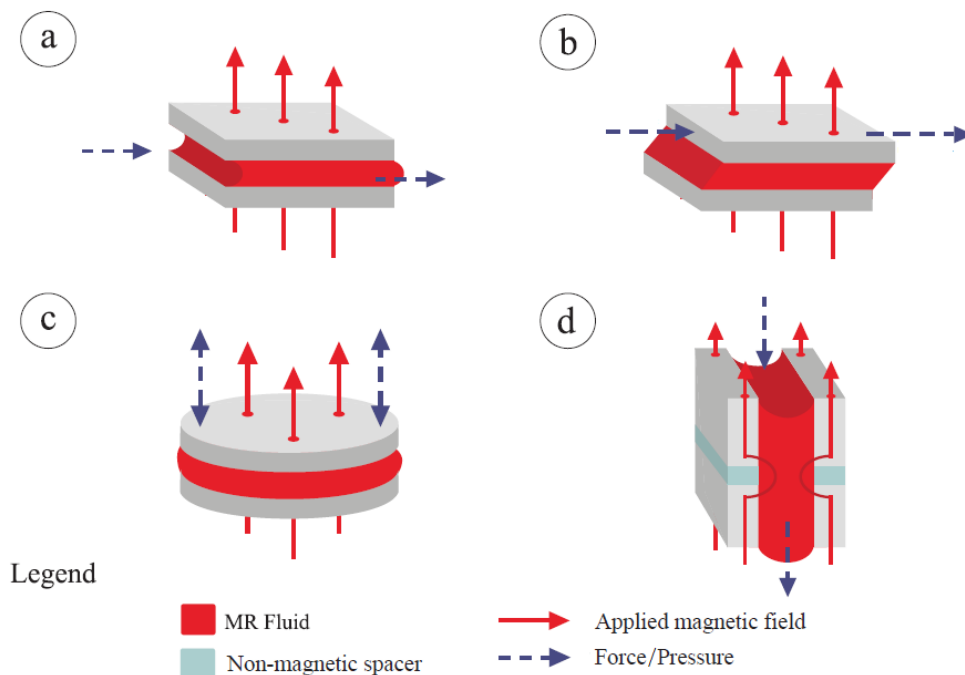


Figure 1.1 - A schematic description of the MR fluid working modes, (a) Flow mode, (b) Shear mode, (c) Squeeze mode, (d) Pinch mode.

1.3. The Magneto-Rheological Brake:

An automotive MRB consists of a rotating disk directly mounted to the wheel shaft and enclosed by a casing. A small gap between the disc and the casing hosts the MR Fluid. MR fluid is under shear operation mode in an MRB. A certain coil winding mechanism is implanted in the device such that the generated magnetic fields are perpendicular to the direction of motion of the disk. Different designs and wiring schemes have been presented in the literature. For example, Park et al. in [5] and [6] anticipated a coil winding rooted around the perimeter of the static casing while Shiao et al. in [7] proposed a multi-pole system. The braking torque generated in the shear mode is controlled by varying the field-dependent yield stress of the MR fluid which is a function of the applied current. The MRB serves unique advantages over other breaking mechanisms as mentioned below:

- An MRB at each wheel can be controlled independently to provide better braking performance.
- Unlike conventional brakes, the working surface area in MRB is the whole disc.
- MRB allows easy implementation of control schemes such as anti-lock braking system (ABS), vehicle stability control (VSC) and electronic parking brake (EPB)...
- Diagnostic of any faults and even behavior modification can be done electronically.
- Environmental advantages: abolishing the use of water polluting brake oil [8] and brake pad dust – particles due to pad wear [9].
- MR fluids are not highly sensitive to moisture contaminants and temperature that might be encountered during manufacture and usage.

Nonetheless, there are some drawbacks associated with MRB systems such as the presence of off-state viscose torque in the absence of applied magnetic field, sealing of MR fluids,

sensitivity to high temperatures (above 150°C) and high cost. Many design concepts have been proposed for MRB. Figure 1.2 shows five major types of MRB designs [4]. The key parameters of different brake designs are the dimensions of the rotating disk and the area in which the magneto-rheological fluid (MRF) is active.

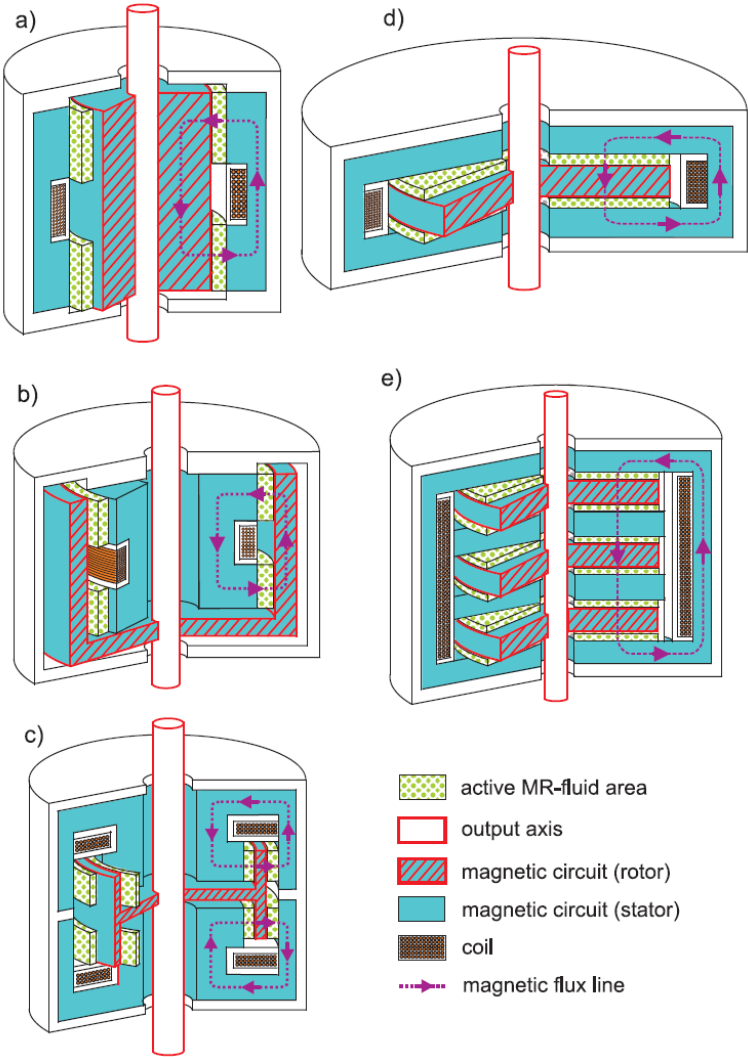


Figure 1.2 - Different types of MRB: (a) drum, (b) inverted drum, (c) T-shaped rotor, (d) disk, and (e) multiple disks [4].

The drum-type MRB has a small radius with long axial dimension. It is the easiest to manufacture amongst the other designs, and it is the least power consuming. The drawback to this design is the high viscous torque generation. The inverted drum design has almost the same characteristics except that the stator is designed to be inside the rotor. The T-shaped rotor design activates a good part of the MR fluid region while having low power consumption, and also produces low viscous torque. The disadvantage of this design is its mechanical complexity and manufacturing. The disk-type MRB design has the advantage of mechanical simplicity along with a low power consumption. Its limitation is the excessive contribution of viscous torque. On the other hand, the multiple disk design demonstrates a lower viscous torque generation and provides the highest dynamic range [4]. It is evident that for automotive applications, since the MRB is to be employed inside the vehicle's wheels, the disk-type MRB is favored due to its compactness and the convenience of its geometric parameters. A two-disk MRB design is selected for this study.

1.4. Review of Relevant Literature:

In this section research, works related to MRB are reviewed and then new recent design concepts to reduce the viscous torque are introduced.

The idea of a "Controllable Brake" was first proposed in 1998 by Carlson [11] in LORD Corporation who holds the patent for the MRB actuator. One of the first applications of the MRB was providing variable torque in exercise bikes [12]. By 2003, many researchers focused on improving the MRB in terms of simplifying its design and fabrication, increasing its response time, making it less noise polluting, and increasing the generated torque [13]. New applications of MRB started to appear like haptic devices [14] and the Series Damper Actuator (SDA) [15]. Later in 2007, the concept of a double-disk MRB was introduced to further enhance the performance of the MRB [16]. Park et al in [5] proposed the application of the MRB in the automotive industry. They

utilized a sliding mode controller to evaluate the performance of the designed MRB. Later in 2007 [6] and 2008 [10], they provided a more enhanced design through multidisciplinary considerations with primary focus on the geometry of the MRB in which optimal design parameters were obtained using the Simulated Annealing algorithm.

The MRB models proposed in [5, 6, 10] considered the Bingham mathematical model which may not render accurate results in high shear rates due to shear thinning/thickening effect. Also, the optimization in [5] and [6] did not involve the zero-current viscous torque. Nguyen et al. in [17] addressed some of these issues and considered Herschel-Bulkley model in their study.

Some optimal designs for disk-type MRBs from the literature are tabulated in Table 1.1. It is noted that in Table 1.1, N_c is the number of coil turns, T_b is the total braking torque, and W_{MRB} is the weight of the MRB. It is also worthy to note that all of these designs were prototyped as 2-disk MRBs.

Table 1.1 - Previous design achievements for the Automotive MRB.

	<i>Math. Model</i>	N_c	<i>MR Fluid</i>	$T_b (N.m)$	$W_{MRB} (kg)$
<i>Park, 2007 [6]</i>	Bingham	80	MRF-132AD	1013	27.9
<i>Karakoc, 2008[10]</i>	Bingham	80	MRF-132DG	1000	27.8
<i>Nguyen, 2010 [17]</i>	Herschel-Bulkley	490	MRF-132DG	1230	56.8

According to Park et al. [5], the limiting values that would allow the MRB to be applied in vehicles are a braking torque of at least 1010 Nm and a brake weight of at most 65 kg. These were the only constraints that previously applied to define an acceptable automotive MRB. All designs

presented in Table 1.1 meet these conditions, but were claimed unacceptable for application in real vehicles due to the presence of the viscous torque.

The major limitation of the conventional MRB design is the viscous torque generation due to the contact between the MR fluid and its interacting surfaces. In addition to the loss of energy, the fluid-surface shearing can negatively affect the fluid's lifetime [18]. Several novel ideas were investigated to limit this contact and to reduce the viscous torque generation. The general concept of the designs is to control the location of the MR fluid and allow it to alternate to different positions between the idle state and the braking state. Usoro et al. [19] adopted the use of gravity to pull the MR fluid to the bottom of the structure as seen in Fig. 1.3(a). When the electromagnet turns on, the MR fluid will be attracted to fill in the active shear gap region.

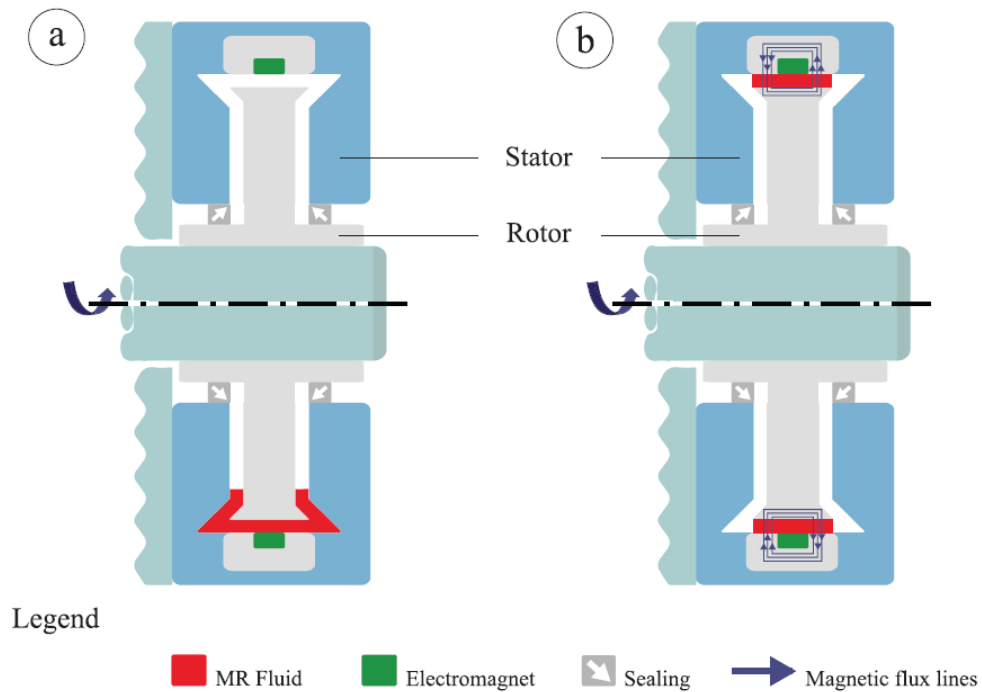


Figure 1.3 – Gravity based MRB design in (a) off state and (b) on state.

The gravity based design indeed reduces the viscous torque produced by the brake; however, there still exists some contact between the MR fluid and the rotor. Guth and Mass [20] proposed a new design that would fully decouple the main parts of the MRB with the aid of centrifugal forces in the idle state by locating the stator inside the rotor. As shown in Fig. 1.4(a), the rotary motion will induce centrifugal forces on the MR fluid which will cause the fluid to be pulled away from the stator in the idle state. When the electromagnet is turned on, the magnetic flux lines will attract the MR fluid and drive it to a location that would make the magnetic flux flow between the stator and the rotor as seen in Fig. 1.4(b).

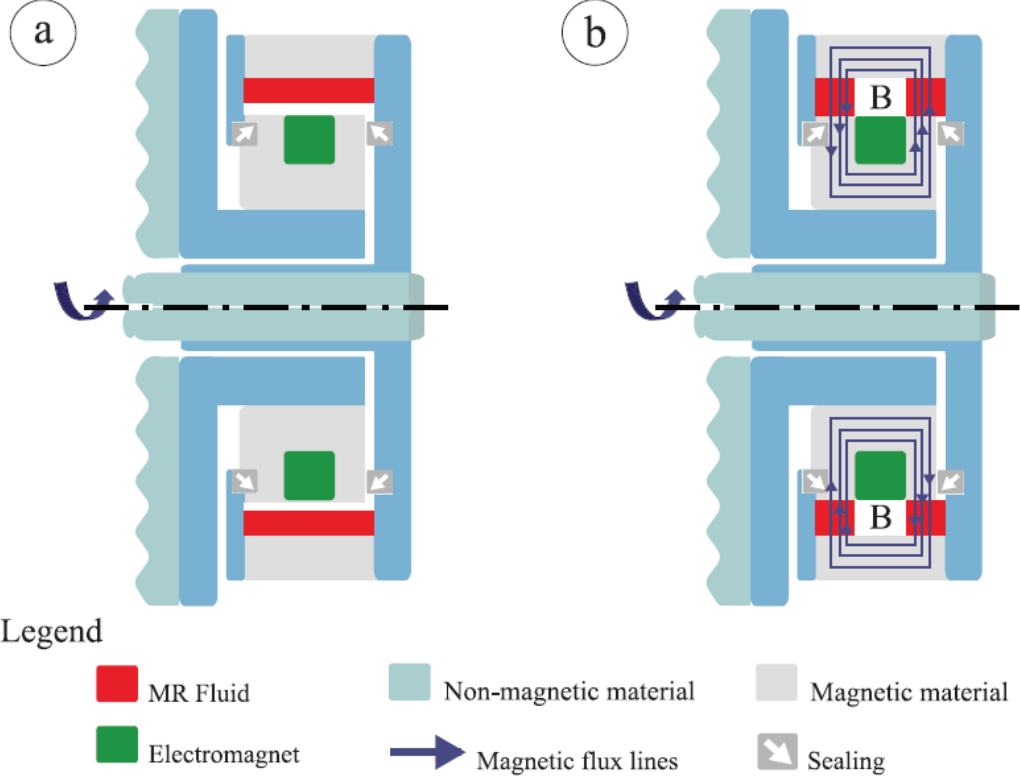


Figure 1.4 – MRB design based on centrifugal forces in (a) off and (b) on states.

The use of permanent magnets to control the location of the MR fluid at different states was later introduced by Guth et al. [21]. Fig. 1.5 shows the concept in which, a permanent magnet (PM) in the rotor ensures that the fluid is locked with the rotor and not touching the stator. When braking is required, the electromagnet (EM) that is mounted with the casing is supplied with current. The magnetic flux lines from the two sources, the PM and the EM, would tend to combine forcing the MR fluid to line up in the shear gap region and generating the braking torque. Guth et al. [21] also presented different control concepts to amount for the brake's de-energized operating behavior by varying the location and number of magnetic sources (permanent or electromagnet) in the MRB design. By modelling and simulation, it was concluded that the design with one PM and one EM (Fig. 1.5) has significantly reduced the torque losses in the off-state and maintained a smooth control of the generated torque in the on state.

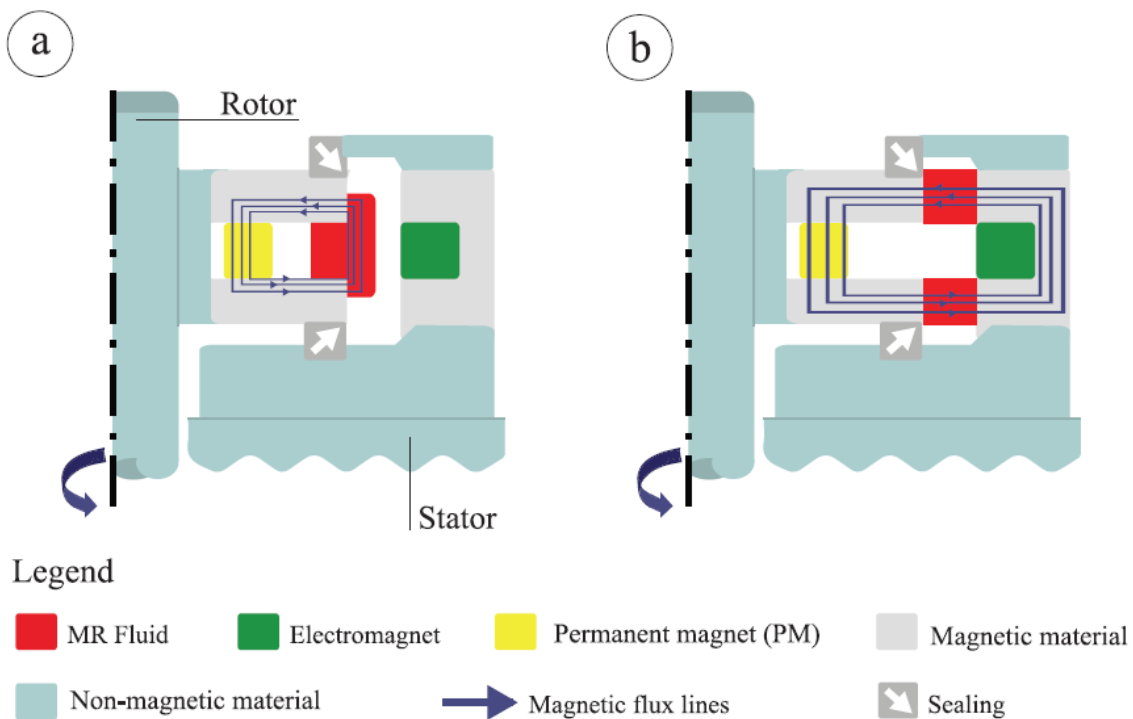


Figure 1.5 – MRB design with PM in (a) off and (b) on states.

1.5. Overall Scope of the Research:

The overall objectives of this research is threefold: 1- to formulate a multi-disciplinary design optimization to performance of a disk-type MRB for real automotive applications through maximizing its dynamic range and torque density while minimizing its inductive time constant and power consumption; 2- To propose a new design concept for disk-type MRBs to eliminate the off-state viscous torque.; 3- To implement the optimally designed MRBs in automotive applications and demonstrate their performance.

1.6. Organization of the Dissertation:

To begin with, an introduction to the topic is presented in Chapter 1. A brief background review of MR Fluids and its applications is presented. Previous works of several research groups around the world on employing the MRB in the automotive industry are summarized in Chapter 1. Furthermore, design concepts in the literature that focus on separating the two working modes of MRB were also presented.

The design variables are introduced, in Chapter 2, to derive the required governing equations for torque analysis using both the Bingham plastic model and the Herschel-Bulkley model. In addition to deriving the governing equations of the conventional MRB design, a novel concept that attempts to provide complete separation of the brake's working modes is introduced and its corresponding torque equations are developed.

Chapter 3 covers the multidisciplinary design approach with primary focus on the magnetic circuit and heat analysis for the suggested designs. The relation between the magnetic flux intensity and current is derived mathematically. After that, a finite element model is developed to validate

the calculations and evaluate the magnetic field intensity and heat distribution in the model. The finite element analysis is performed using an open-source software named FEMM.

In Chapter 4, the obtained information from previous chapters has been used to define an objective function of the design optimization problem and its constraints. The overall objective is to maximize the dynamic range and torque to volume ratio of the MRB while acquiring minimum power consumption. In the design optimization process, a combined Genetic Algorithm and Sequential Quadratic Programming are employed using MATLAB software.

After the optimal parameters are obtained, a dynamic model of the vehicle with MRB is presented in Chapter 5. A PID controller is applied to prevent wheel lock-up (sliding) and to investigate the performance of the designed MRB in a real vehicle application on different road conditions.

Finally, conclusions are drawn in Chapter 6. The major contributions and limitations of this work are listed, and future studies to further enhance the design are recommended.

CHAPTER 2

MAGNETO-RHEOLOGICAL BRAKE-DAMPING TORQUE

FORMULATION

2.1. Introduction:

In this chapter, first a mathematical formulation to derive the braking torque for a conventional two-disk MRB design is presented based on both Bingham and Herschel-Bulkley models. A novel MRB design is then proposed for the purpose of increasing the brake's dynamic range. The proposed design examines a novel mode separation technique to completely eliminate any viscous torque generation. The designs are demonstrated and the geometric variables are defined.

2.2. Derivation of the Braking Torque – Conventional MRB:

For the purpose of deriving the torque equation, a preliminary Computer Aided Design (CAD) model of the MRB has been drawn using the CATIA software as shown in Fig. 2.1. This is a 2-disk MRB similar to that used in Ref. [10]. The main geometrical parameters of the selected MRB are also shown in Fig. 2.1. It should be noted that the shaft with thickness b_s is proposed to mount on the wheel axle using the car wheel bolts – the same manner as a conventional hydraulic brake discs are connected. The CAD model serves as the reference to derive the torque equations. The total braking torque is derived according to two regions of the MR fluid: the “active” region, where the MR fluids and magnetic field intersect, and the “inactive” region, where the MR fluid is unaffected by the magnetic field.

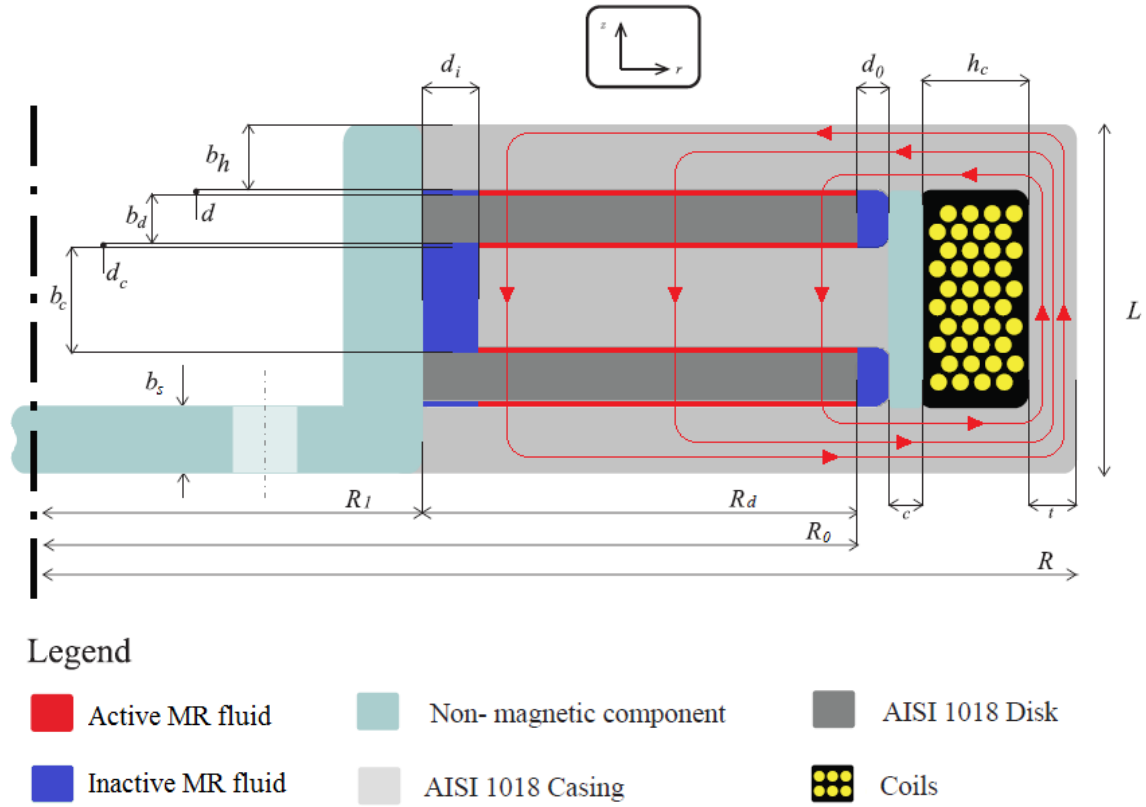


Figure 2.1 – Sectioned dimensioning of the MRB.

Considering the active region, the moment, per one MR fluid gap, due to the friction at a point of radius r on the disk is expressed as [17]:

$$dT = 2\pi r^2 \tau_{z\theta} dr + 2\pi r^2 \tau_{r\theta} dz \quad (1)$$

It is observed that the gap sizes of the MR fluid (d and d_c) are much smaller than the disc radius. Also, the stress $\tau_{z\theta}$ is much larger than $\tau_{r\theta}$; thus, the second term in Eq. (1) can be ignored. The induced torque for all the MRF gaps in the active region can be estimated after integration over the pertinent areas as:

$$T_{act} = 4\pi \int_{R_1}^{R_0} r^2 \tau dr + 4\pi \int_{R_{c1}}^{R_0} r^2 \tau dr \quad (2)$$

where, according to Figure 2.1, $R_0 = R_1 + R_d$, $R_{c1} = R_1 + d_i$ and $\tau = \tau_{z\theta}$ is the shear stress in z - θ plane. According to the Herschel-Bulkley model, the shear stress developed in the MR fluid can be represented as:

$$\tau = (\tau_y + K|\dot{\gamma}|^n) \text{sgn}(\dot{\gamma}) \quad (3)$$

where τ_y is the field dependent yield strength which is the function of the applied magnetic field intensity, H , and $\dot{\gamma}$ is the shear strain rate of the MR fluid, which can be approximated as:

$$\dot{\gamma} = \frac{r\dot{\theta}}{d_{MR}} \quad (4)$$

where $\dot{\theta} = \omega$ is the angular velocity of the shaft and the d_{MR} is the MR fluid gap; d or d_c . The parameters K and n are the consistency and flow behavior indexes. They are properties of the MR fluid and may vary as a function of the surrounding magnetic flux density. A recent study by Arief et al [22] shows that for a particular MR fluid, at shear rates of over 200 s^{-1} , these parameters are nearly constant independent of the change in magnetic field intensity. Here, MRF-132DG from Lord Corporation has been utilized. To evaluate parameters K and n in the absence of magnetic field (K_0 and n_0), a quadratic equation is fitted into the shear stress versus shear rate curve given for MRF-132DG [23] using the least square method. The experimental data point extracted from data sheet of MRF-132DG [23] (solid square boxes) together with the curve fitted quadratic equation is shown in Fig. 2.2. The quadratic relation has been found to be:

$$\tau = -9 \times 10^{-6} \dot{\gamma}^2 + 0.1089 \dot{\gamma} + 10.821 \quad (5)$$

which gives a coefficient of determination (R^2) of 0.9991.

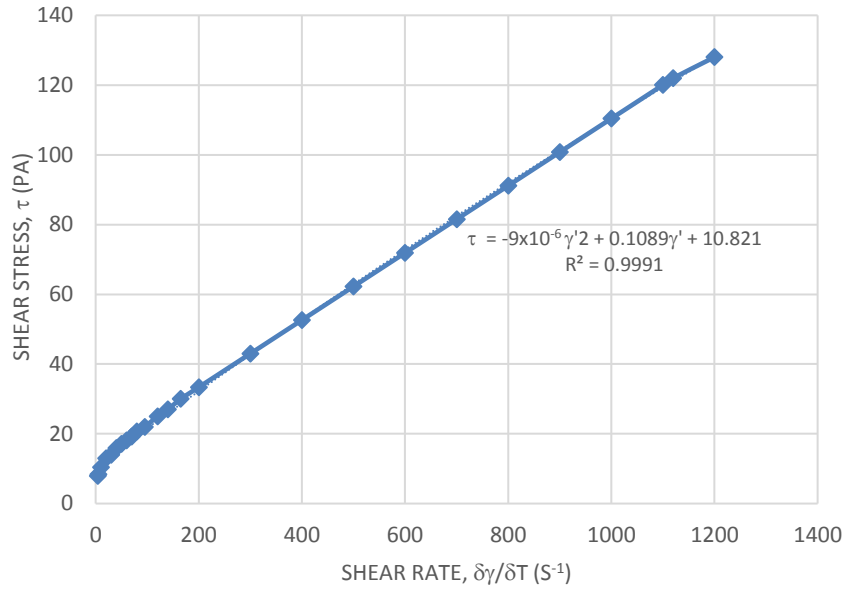


Figure 2.2 – Shear stress as a function of Shear rate for MRF-132DG at 0A.

Since the brake operates at positive shear rates, the Herschel-Bulkley model equation can be re-written as:

$$\tau = \tau_y + K_0 \dot{\gamma}^{n_0} \quad (6)$$

Now, equating Eq. (5) and Eq. (6) yields $\tau_{y0} = 10.821 \text{ Pa}$; and:

$$K_0 \dot{\gamma}^{n_0} = -9 \times 10^{-6} \dot{\gamma}^2 + 0.1089 \dot{\gamma} \quad (7)$$

In order to estimate the parameters K_0 and n_0 , two values of $\dot{\gamma}$, 200 and 400 s^{-1} are chosen, thus:

$$K_0 (200)^{n_0} = 21.42$$

$$K_0 (400)^{n_0} = 42.12$$

which yields: $K_0 = 0.1219$ and $n_0 = 0.9755$.

It is noticed that K_0 is approximately equal to MRF-132DG's viscosity, μ_0 , given in the manufacturer's manual [23], and n_0 is close to 1. These approximations leaves the Herschel-Bulkley with the following representation:

$$\tau = \tau_y + \mu_0 \dot{\gamma} \quad (8)$$

which is the representation of the Bingham mathematical model.

Thus, in the absent of magnetic field the Bingham model can well represent the shear stress-shear strain rate behavior of the MR fluids.

2.3. Torque equations based on the Bingham Plastic Model:

The Bingham model is a simplified mathematical model that is accurate for calculating the shear stress of the MR fluid on low shear rates. If the MR brake is to operate at high shear rates, the Bingham model is believed to overestimate the generated braking torque [4] due to the shear thinning behavior of MR fluids. Substituting Eq. (4) into Eq. (8) and then back into Eq. (2) yields:

$$\begin{aligned} T_{act} = & 4\pi \int_{R_1}^{R_0} r^3 \mu_0 \frac{\dot{\theta}}{d} dr + 4\pi \int_{R_1}^{R_0} r^2 \tau_y dr \\ & + 4\pi \int_{R_{c1}}^{R_0} r^3 \mu_0 \frac{\dot{\theta}}{d_c} dr + 4\pi \int_{R_{c1}}^{R_0} r^2 \tau_y dr \end{aligned} \quad (9)$$

After integration, the torque equation in Eq. (9) can be written as:

$$T_{act} = T_H + T_\mu \quad (10)$$

where T_H is the brake torque generated due to the applied magnetic field and T_μ is the brake torque generated due to viscous friction of the MR fluid:

$$T_H = \frac{4\pi}{3} (2R_0^3 - R_1^3 - R_{c1}^3) \tau_y(H) \quad (11)$$

$$T_\mu = \pi\mu_0 \left(\frac{R_0^4 - R_1^4}{d} + \frac{R_0^4 - R_{c1}^4}{d_c} \right) \dot{\theta} \quad (12)$$

The preceding equations estimated the retarding torque resulting from the friction between the MR fluid and the rotating disk in the active region. Likewise, the friction torque developed in the inactive regions can be derived as:

$$T_{inact} = 2\pi(R_1)^2 b_a \left(\tau_{y0} + \mu_0 \frac{(R_1)\dot{\theta}}{d_i} \right) + 4\pi R_0^2 b_d \left(\tau_{y0} + \mu_0 \frac{R_0\dot{\theta}}{d_0} \right) \quad (13)$$

where $b_a = b_c + 2d_c$. Eq. (13) can be rearranged to:

$$T_{inact} = 2\pi\mu_0 \left[\frac{2R_0^3 b_d}{d_0} + \frac{R_1^3 b_a}{d_i} \right] \dot{\theta} + 2\pi\tau_{y0} [2R_0^2 b_d + R_1^2 b_a] \quad (14)$$

where τ_{y0} is the MR fluid yield stress at zero magnetic field.

2.4. MR Fluid Field-Dependent Yield Stress:

The variation of yield stress as a function of magnetic flux intensity has been obtained experimentally for MRF-132DG and is provided in the manufacturer's specifications [23] which has been displayed in Fig. 2.3 using solid circles. A quadratic equation has then been curve fitted to the experimental data, using least square method, to mathematically describe the variation of yield stress versus the applied magnetic field. The resulting quadratic equation for the yield stress of this particular MR fluid is shown in Figure 2.3 as dash line and can be expressed as:

$$\tau_y = -0.0007H^2 + 0.3574H + 0.01 \quad (15)$$

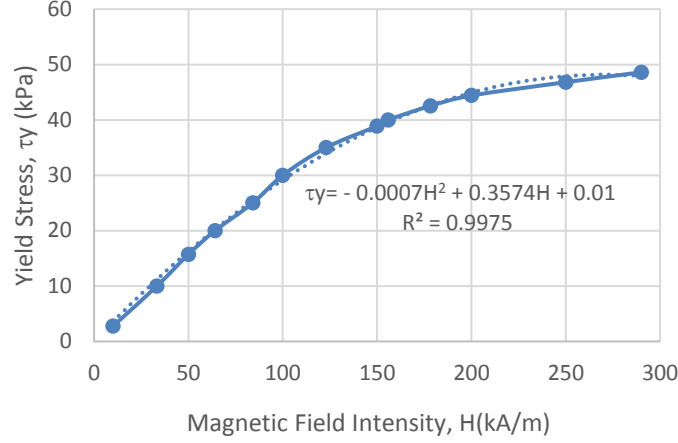


Figure 2.3 – Yield Stress versus Magnetic Field Strength for MR-132DG [18].

It is noted that the Eq. (15) gives the coefficient of determination (R^2) of 0.9975.

2.5. Torque Equations based on the Herschel-Bulkley model:

The Herschel-Bulkley mathematical model is used for a more accurate estimation of the torque equations with fewer assumptions. In this model, the variation of the field-dependent rheological properties, K , n and τ_y for different magnetic flux densities, B , may be expressed as [24]:

$$K = K_\infty + (K_0 - K_\infty)(2e^{-B\alpha_{SK}} - e^{-2B\alpha_{SK}}) \quad (16)$$

$$n = n_\infty + (n_0 - n_\infty)(2e^{-B\alpha_{Sn}} - e^{-2B\alpha_{Sn}}) \quad (17)$$

$$\tau_y = \tau_{y\infty} + (\tau_{y0} - \tau_{y\infty})(2e^{-B\alpha_{STy}} - e^{-2B\alpha_{STy}}) \quad (18)$$

where K_0 , n_0 and τ_{y0} are the properties at zero magnetic field as discussed before, K_∞ , n_∞ and $\tau_{y\infty}$, are the saturation values of the properties and α_{SK} , α_{Sn} and α_{STy} are related to the torque. For Lord MR fluid MRF-132DG these parameters are reported by Nguyen and Choi [17] to be $0.22 Pa.s^n$ and 0.917 for K_0 and n_0 , $3900Pa.s^n$ and 0.25 for K_∞ and n_∞ , and $5 T^{-1}$ and 32 for α_{SK} and α_{Sn} ,

respectively. For MR fluid MRF-132DG, yield stress in the absence of magnetic field, τ_{y0} , is $10.821 Pa$, as obtained in the previous section and yield saturation limit, $\tau_{y\infty}$, and α_{STy} are also reported to be $50 kPa$ and $2 T^{-1}$, respectively [17]. Substituting the relative parameters in Herschel-Bulkley model in Eq. (3) yields the determination of MR fluid's shear stress at any magnetic flux density.

A similar approach has been used for MRF-132DG by Nguyen and Choi [17] except for different values for the yield stress in the absence of magnetic field and at its saturation limit. The result of shear stress versus shear rate for the MR fluid MRF-132DG in the absence of magnetic field and its comparison with those based on experimental data from Lord Corporation and Nguyen and Choi [17] is shown below in Figure 2.4. It can be realized that results agree very well with those reported experimental data.

Eq. (16), Eq. (17) and Eq. (18) combined with Eq. (3) can now be utilized to obtain the shear stress as a function of shear rate at different magnetic flux densities. Figure 2.5 shows the variation of shear stress with respect to shear rate for MR fluid MRF-132DG for flux densities ranging from $0.25T$ to $1.5T$. For validation, it can be seen from Fig. 2.3, that the yield shear stress reaches its saturation limit of $50 kPa$ at nearly $300 kA/m$, which is equivalent to a flux density of $1T$ [23]. From Fig. 2.5, at $B=1T$, it can be realized that assuming a linear relationship (the Bingham model), the yield shear stress is near to $50 kPa$.

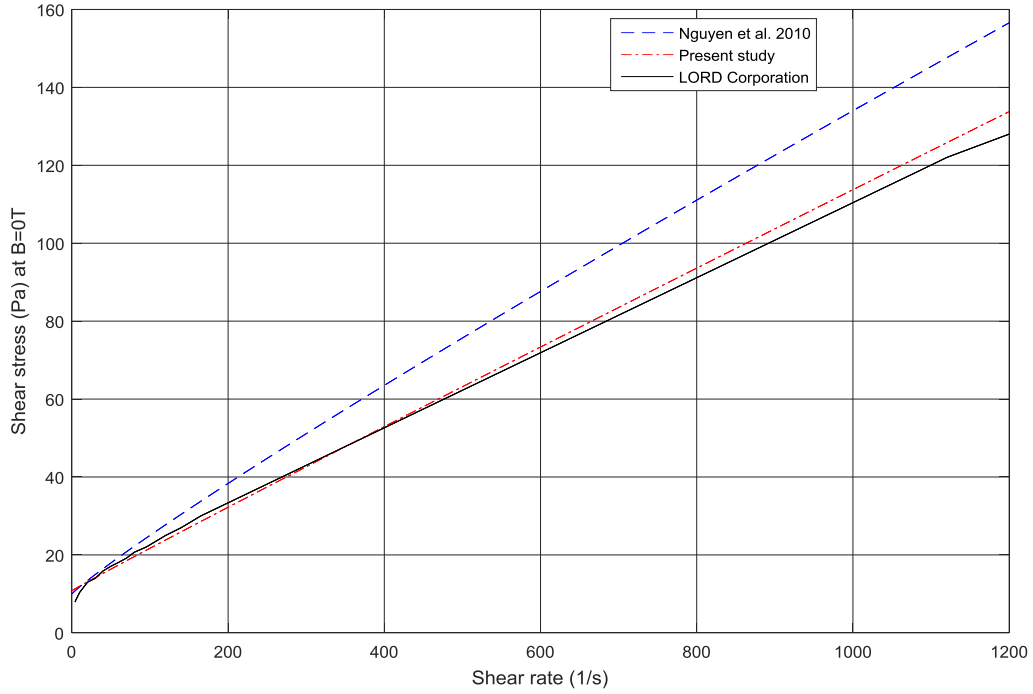


Figure 2.4 – Comparison of Shear stress versus Shear rate for MRF-132DG at 0A.

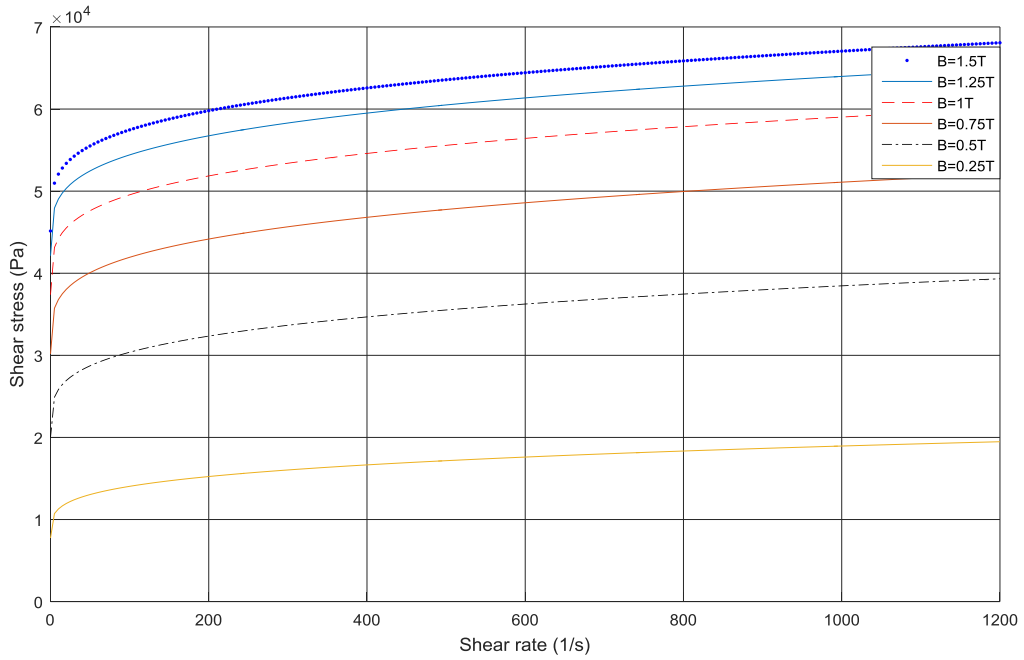


Figure 2.5 – Shear stress vs. Shear rate at different magnetic flux densities.

The experimental relation between the magnetic flux density and the magnetic field intensity for MRF-132DG is reported in [23] and is shown in Figure 2.6 (solid diamonds). The

least square criteria is again used to map a fourth order polynomial (dashed line in Figure 2.6) over the experimental data with an acceptable coefficient of determination (R^2) of 0.9988 as:

$$B = -2.127E-11H^4 + 3.73E-08H^3 - 2.34E-05H^2 + 0.007585H \quad (19)$$

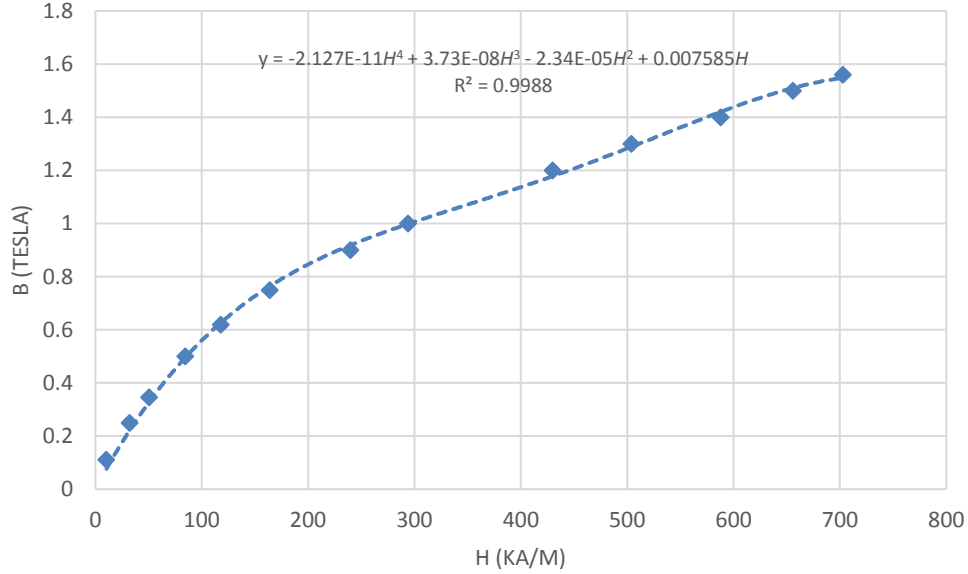


Figure 2.6 – Magnetic field Density versus Intensity for MRF-132DG.

Using the Herschel-Bulkley model, similar to that of the Bingham plastic model, the torque in the active region can be expressed as:

$$T_{act} = 4\pi K \int_{R_1}^{R_0} r^{2+n} \frac{\dot{\theta}^n}{d^n} dr + 4\pi \int_{R_1}^{R_0} r^2 \tau_y dr \quad (20)$$

$$+ 4\pi K \int_{R_{c1}}^{R_0} r^{2+n} \frac{\dot{\theta}^n}{d_c^n} dr + 4\pi \int_{R_{c1}}^{R_0} r^2 \tau_y dr$$

Solving the integrals in Eq. (20) yields:

$$T_{act} = \frac{4\pi K}{(n+3)d^n} (R_0^{3+n} - R_1^{n+3}) \dot{\theta}^n + \frac{4\pi}{3} (R_0^3 - R_1^3) \tau_y \quad (21)$$

$$\frac{4\pi K}{(n+3)d_c^n} (R_0^{3+n} - R_{c1}^{n+3}) \dot{\theta}^n + \frac{4\pi}{3} (R_0^3 - R_{c1}^3) \tau_y$$

Equation (21) can also be represented as $T_{act} = T_H + T_\mu$, similar to that in Eq. (10) in which the brake torque generated due to the applied magnetic field, T_H , and the brake torque generated due to viscous friction of the MR fluid, T_μ , are:

$$T_H = \frac{4\pi}{3} (2R_0^3 - R_1^3 - R_{c1}^3) \tau_y \quad (22)$$

$$T_\mu = \frac{4\pi K}{n+3} \left(\frac{R_0^{3+n} - R_1^{n+3}}{d^n} + \frac{R_0^{3+n} - R_{c1}^{n+3}}{d_c^n} \right) \dot{\theta}^n \quad (23)$$

In the inactive region, the torque generated is derived as:

$$T_{inact} = 2\pi K_0 \left[2b_d \frac{R_0^{2+n_0}}{d_0^{n_0}} + b_a \frac{R_1^{2+n_0}}{d_i^{n_0}} \right] \dot{\theta}^{n_0} \quad (24)$$

$$+ 2\pi \tau_{y0} [2R_0^2 b_d + R_1^2 b_a]$$

where $b_a = b_c + 2d_c$, and τ_{y0} is the MR fluid yield stress at zero magnetic field. It is noted that the rheological properties K_0 and n_0 are chosen in Eq. (24) since there will be no magnetic flux density at the inactive region; i.e. $B=0$ Tesla.

Now, the total braking force (T_b) of the MRB, whether for the Bingham model or the Herschel-Bulkley model, can be obtained by summing the two derived torque equations in active and inactive regions as:

$$T_b = T_H + T_\mu + T_{inact} \quad (25)$$

The dynamic range (DR) of the MRB is defined by the ratio of torque in the “on” state ($i \neq 0$) over the torque in the “off” state ($i = 0$) as:

$$DR = \frac{T_b}{T_\mu + T_{inact} + T_{0i}} \quad (26)$$

where T_{0i} is the residual torque from T_H at the absence of magnetic field (zero current) due to the presence of τ_y .

2.6. Torque Equations for a Multiple Disk MRB:

Using similar derivation methods as described in previous sections, the general equation for a disk-type MRB with N disks with design similar to the present study in Figure 2.1 (having a core from the casing between each pair of disks) can be derived as follows:

- For the Bingham model:

$$T_b = \frac{2N\pi}{3} (2R_0^3 - R_1^3 - R_{c1}^3) \tau_y + 2N\pi\mu_0 \left(\frac{R_0^4 - R_1^4}{d} + \frac{R_0^4 - R_{c1}^4}{d_c} \right) \dot{\theta} \\ + N\pi\mu_0 \left[\frac{2R_0^3 b_d}{d_0} + \frac{(R_1 + a)^3 b_a}{d_i} \right] \dot{\theta} + N\pi\tau_{y0} [2R_0^2 b_d + (R_1 + a)^2 b_a] \quad (27)$$

- For Herschel-Bulkley model:

$$T_b = \frac{2N\pi}{3} (2R_0^3 - R_1^3 - R_{c1}^3) \tau_y + \frac{2N\pi K}{n+3} \left(\frac{R_0^{3+n} - R_1^{n+3}}{d^n} + \frac{R_0^{3+n} - R_{c1}^{n+3}}{d_c^n} \right) \dot{\theta}^n \\ + N\pi K_0 \left[2b_d \frac{R_0^{2+n_0}}{d_0^{n_0}} + b_a \frac{(R_1 + a)^{2+n_0}}{d_i^{n_0}} \right] \dot{\theta}^{n_0} + N\pi\tau_{y0} [2R_0^2 b_d + (R_1 + a)^2 b_a] \quad (28)$$

It should be noted that that the least value for number of disks to implement the current design is two. For the conventional MRB design with one disk, the total torque generated is described as:

- For the Bingham model:

$$T_b = \frac{2\pi}{3}(R_0^3 - R_1^3)\tau_y + 2\pi\mu_0\left(\frac{R_0^4 - R_1^4}{d}\right)\dot{\theta} + 2\pi b_d R_0^2 \tau_{y0} + 2\pi\mu_0 b_d \frac{R_0^3}{d_0} \dot{\theta} \quad (29)$$

- For Herschel-Bulkley model:

$$T_b = \frac{2\pi}{3}(R_0^3 - R_1^3)\tau_y + \frac{2\pi K}{n+3}\left(\frac{R_0^{3+n} - R_1^{n+3}}{d^n}\right)\dot{\theta}^n + 2\pi K_0 b_d \frac{R_0^{2+n_0}}{d_0^{n_0}} \dot{\theta}^{n_0} + 2\pi R_0^2 b_d \tau_{y0} \quad (30)$$

2.7. Novel Decoupled Design:

Inspired by the design approaches proposed by Guth et al. [21], an MRB design that would be practical for use in the automotive industry has been proposed. The main purpose of this design is to completely eliminate the MR fluid–rotor surface contact in the off state. The decoupling of MR fluids with rotor surface in the off-state can be achieved by integrating permanent magnets (PM) on parts of the casing as shown in Fig. 2.7. The PM can practically attract the specified volume of the MR fluid into a neighboring gap to lock them with the stator and prevent their contact with the rotor. O-ring seals are placed at the edges of the active region to insure the fluid remains in the active shear gap region.

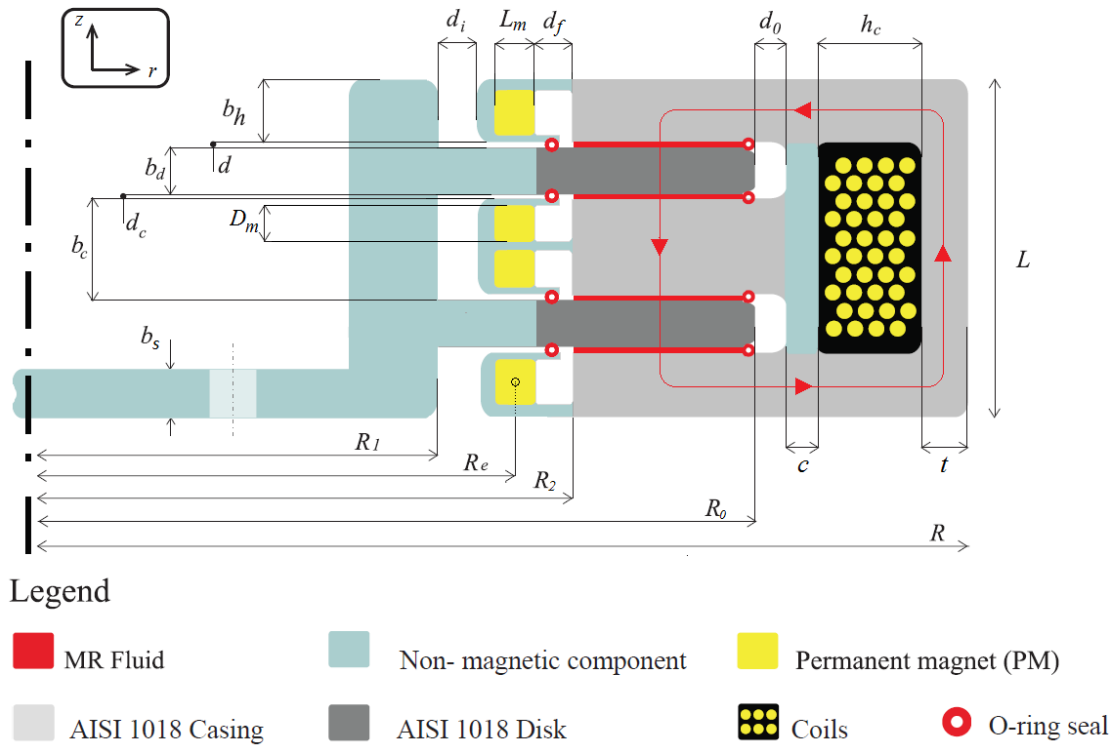


Figure 2.7 – Proposed Decoupled Design.

The design parameters presented in Figure 2.7 for this proposed design are equivalent to those of the conventional MRB design, in addition to three more parameters: L_m , D_m and R_2 . L_m and D_m are dimensions (length and thickness) of the permanent magnets. The parameter R_2 is introduced to define the lower radius of the shear gap region, where the MR fluid are situated in the ‘on’ state. R_e is the effective radius of the PM; calculated as: $R_e = R_2 - d_f - L_m/2$. Figure 2.8 demonstrates the off-state and on-state configurations of the proposed novel MRB design.

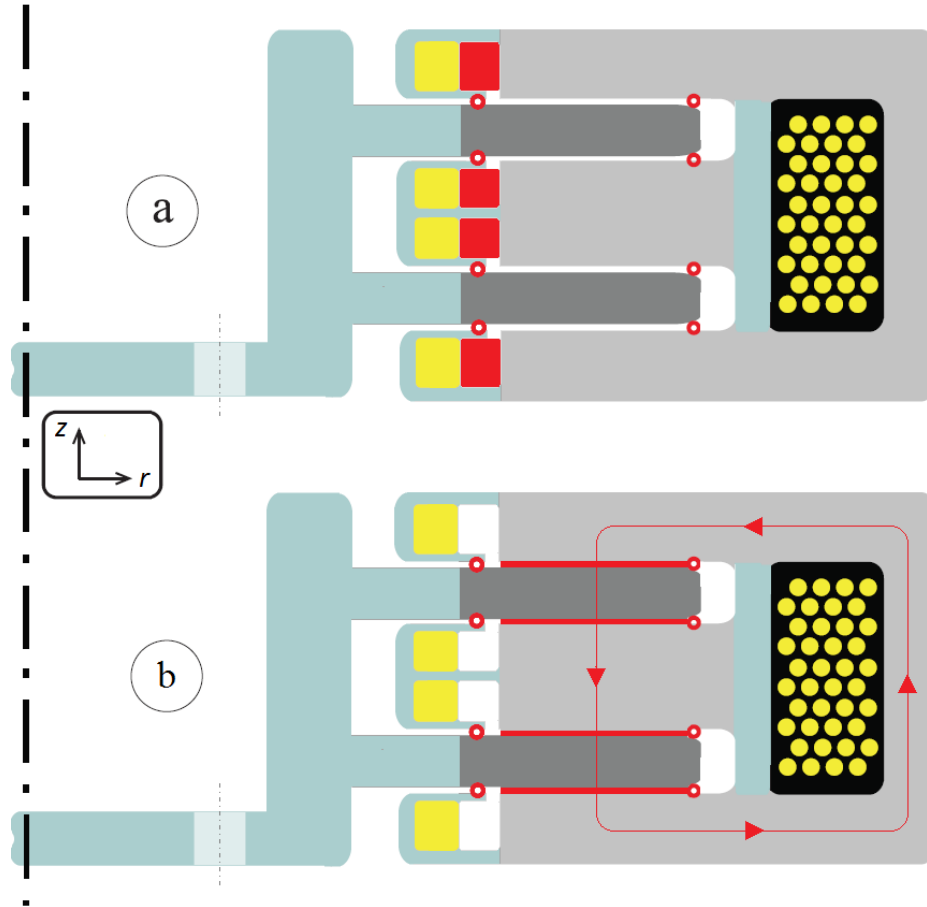


Figure 2.8 – Novel de-coupling design in (a) off-state and (b) on state.

As it can be seen in Figure 2.8, four permanent magnets are embedded in the side walls and core section of the stator casing. The role of the magnets is to attract the MR fluids to fill the neighboring gaps in the off-state as shown in Figure 2.8(a). In this case, the MR fluid will be merged with the casing and completely separated from the brake's rotor. However, in the on-state configuration, the main large electromagnet embedded in the outer radial surface of the casing is supplied with the current creating a strong magnetic field that will pull the MR fluid out of the gaps and into the shear gap region as shown in Figure 2.8 (b). In this research study, the transition

phase between the on and off state is assumed to be perfect. A justification of this assumption is given later in Chapter 3.

The complete separation in this design leads to near elimination of viscous torque through preventing any friction in the shear gap region in the idle state. The torque equations for this designs are estimated using the same approach as that of the conventional MRB in previous sections except R_1 and $R_{c1}=R_1+d_i$ are replaced with R_2 in Eq. (2). The torque's two corresponding components using Bingham and Herschel-Bulkley models can be given as:

- For the Bingham model:

$$T_H = \frac{8\pi}{3} (R_0^3 - R_2^3) \tau_y \quad (31)$$

$$T_\mu = \pi\mu_0 (R_0^4 - R_2^4) \left(\frac{1}{d} + \frac{1}{d_c} \right) \dot{\theta} \quad (32)$$

- For Herschel-Bulkley model:

$$T_H = \frac{8\pi}{3} (R_0^3 - R_2^3) \tau_y \quad (33)$$

$$T_\mu = \frac{4\pi K}{n+3} (R_0^{3+n} - R_2^{n+3}) \left(\frac{1}{d^n} + \frac{1}{d_c^n} \right) \dot{\theta}^n \quad (34)$$

For the proposed design, with no viscous torque, the dynamic range of the design is nothing but the total braking torque which for the case Herschel-Bulkley model can be expressed as:

$$DR = T_b = \frac{8\pi}{3} (R_0^3 - R_e^3) \tau_y + \frac{4\pi K (R_0^{3+n} - R_e^{n+3})}{n+3} \left(\frac{1}{d^n} + \frac{1}{d_c^n} \right) \dot{\theta} \quad (35)$$

2.8. Summary:

In this chapter, two MRB designs are introduced: a conventional 2-disk MRB and a novel 2-disk MRB design. The novel MRB design is proposed for the purpose of increasing the brake's dynamic range. The proposed design examines a novel mode separation technique to completely eliminate any viscous torque generation. The designs are demonstrated and the geometric variables are defined. The mathematical formulation to derive the braking torque for both designs is presented based on both Bingham and the Herschel-Bulkley models for single and multiple disk configurations. Magneto-static and heat analysis are discussed in the following chapter.

CHAPTER 3

MR BRAKE MAGNETIC CIRCUIT AND TEMPERATURE

ANALYSIS

3.1. Introduction:

The aim of this chapter is to develop an analytical model of the MRB's magnetic circuit and heat generation. A preliminary design with dummy variables is introduced and the materials corresponding to the parts of the MRB are defined. A magnetic circuit analysis is then performed followed by a heat analysis. The resulting models are then validated using the developed finite element model.

3.2. Preliminary Design:

It is required to specify an initial design that would serve as a reference to perform the magnetic circuit and temperature analysis on the MRB. With reference to Figure 2.1 of Chapter 2, the geometric variables for the initial design are chosen similar to those reported in Ref. [25] for the conventional MRB and are tabulated in Table 3.1.

Table 3.1 - Geometric variables for the preliminary design of the MRB.

<i>Design Variables</i>	<i>Value (cm)</i>
R_l	13.06
R_d	5.05
c	0.30
d	0.13
d_c	0.13
d_0	0.13
d_i	0.13
h_c	1.48
t	1.22
b_h	0.65
b_d	0.60
b_c	0.70

As for the material assignments, the MR fluid considered for the present study is LORD Corporation's MRF-132DG. The disk teeth and the casing should be made of magnetic material with high permeability for easier passage of magnetic flux. Low carbon steel AISI 1018 due to its high permeability, availability and cost [16] is a good selection for the current application. For the non-magnetic core and the disk shaft, a non-magnetic material is required. Accordingly, aluminum alloy 1100 is selected for its availability, good machinability and low weight (density of 2.71 g/cm^3). The wires wrapped around the nonmagnetic bobbin of the MRB's electromagnet are selected to be the American Wire Gauge - AWG 21 – of diameter 0.7239 mm which is made of copper alloy of density nearly 8.87 g/cm^3 .

3.3. Analytical Magnetostatic Circuit Analysis - Conventional MRB:

The analysis of the magnetic circuit of the magneto-rheological brake is required to calculate the relationship between magnetic the induced field intensity and applied current in the MR fluid active region gap. According to the Ampere's law, we may write:

$$\sum H_k l_k = N_c i \quad (36)$$

where H_k and l_k are the magnetic field intensity and effective length of the k -th link in the circuit. N_c is the number of turns of the coil and i is the applied current.

The magnetic flux is conserved and its continuity is described in the circuit as:

$$\Phi = B_k A_k \quad (37)$$

where Φ is the magnetic flux, A_k is the cross-sectional area of the k -th link, and B_k is the magnetic flux density, described by:

$$B_k = \mu_{sp} \mu_k H_k \quad (38)$$

in which $\mu_{sp} = 4\pi \times 10^{-7} TmA^{-1}$ is the constant magnetic permeability of free space and μ_k is the relative permeability of the k -th link.

Finding the exact solution for the magnetic circuit is very challenging. However, an approximate solution can be obtained for the given magnetic circuit of the magneto-rheological brake assuming uniformity of the magnetic field and linear relationship between magnetic flux density and magnetic field intensity (constant relative permeability). The approximate circuit with related magnetic links is presented in Figure 3.1. It should be noted that the magnetic field intensity distribution is not the same throughout the whole area where the MR fluid lies. Considering the fact that not all the disk area is “active,” the dimension r_a is introduced to represent the length of the inactive region, assumed as: $r_a = d_i$. The effective lengths of the 12 links considered in the magnetic circuit shown in Figure 3.1 with respect to geometrical parameters can be described as:

$$\left\{ \begin{array}{l} l_1 = L - b_h \\ l_2 = l_{12} = (R - R_1) - d_i - \frac{R_0 - R_1 - d_i}{2} - \frac{t}{2} \\ \quad = R - \frac{R_0 + R_1 + d_i + t}{2} \\ l_3 = l_{11} = \frac{b_h}{2} \\ l_4 = l_{10} = d \\ l_5 = l_9 = b_d \\ l_6 = l_8 = d_c \\ l_7 = b_c \end{array} \right. \quad (39)$$

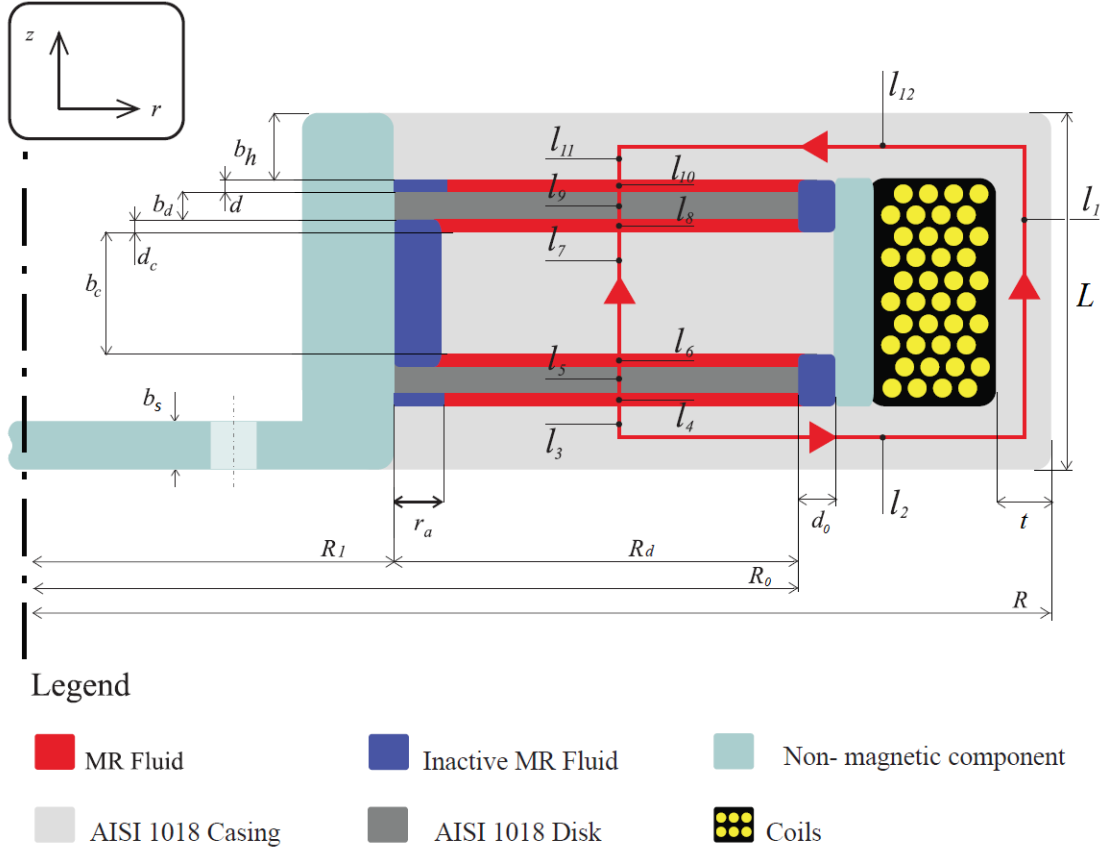


Figure 3.1 – The Magnetic Circuit of the MRB.

The links' corresponding cross-sectional areas are:

$$\begin{cases} A_1 = \pi[R^2 - (R-t)^2] \\ A_2 = A_{12} = \pi b_h(R-t + R_1 + d_i) \\ A_3 = A_4 = \dots = A_{11} = \pi[R_0^2 - R_{c1}^2] \end{cases} \quad (40)$$

It is noted that for the 2nd and 12th link, as the effective length gets closer to the center of rotation of the MRB, the cross-sectional area is linearly decreasing from $2\pi(R-t)b_h$ to $2\pi(R_1 + d_i)b_h$.

Here, for the ease of calculation, the median value for the total cross-sectional area variations is taken and assumed constant over the two links.

In the MRB design, it is assumed that the magnetic components of the brake are made of the same steel type, low carbon steel AISI 1018. Thus, considering Eq. (36) one can write:

$$N_c i = (l_1 + l_2 + l_3 + l_5 + l_7 + l_9 + l_{11} + l_{12})H_s + (l_4 + l_6 + l_8 + l_{10})H \quad (41)$$

H_s and H are the magnetic field in the steel and MR fluid links, respectively. Now using the relationships in Eq. (37) and Eq. (38), we can also write:

$$H_s = \frac{\Phi}{\mu_{sp}\mu_s A_s} = \frac{B_f A_f}{\mu_{sp}\mu_s A_s} \quad (42)$$

Substituting Eq. (38) for B_f into Eq. (42) yields the relationship between the magnetic field intensities of the steel and the MR fluid as:

$$H_s = \left(\frac{\mu_f A_f}{\mu_s A_s} \right) H \quad (43)$$

where A_s and A_f are effective cross-sectional areas in relative steel and MR fluid links, respectively, and μ_s and μ_f are relative permeability of the steel and MR fluid, respectively. The relative permeability of the magnetic fluid, MRF 132-DG, and the metallic component, low carbon steel AISI 1018 are properties that may vary with the magnetic field intensity. The values of relative permeability of MR fluids are in the order of 5, while that of iron is in the order of 5000 [4]. For the ease of calculation, they are assumed to be constant and are estimated as $\mu_s \approx 1000\mu_f$.

Finally, after substituting Eq. (43) into Eq. (41), the magnetic field intensity in the MR fluid gaps can be approximated as:

$$H = \frac{N_c}{\left(\frac{\mu_f}{\mu_s}\right)\left(\frac{l_1 A_3}{A_1} + \frac{2l_2 A_3}{A_2} + 2l_3 + 2l_5 + l_7\right) + 2l_4 + 2l_6} i \quad (44)$$

Once the magnetic field intensity is calculated, the magnetic flux density, B , can be numerically estimated using Eq. (19) in Chapter 2 for the MR fluid MRF 132-DG.

To estimate the number of wires that can fit inside the available coil area, consider the wire area box proposed in Figure 3.2.

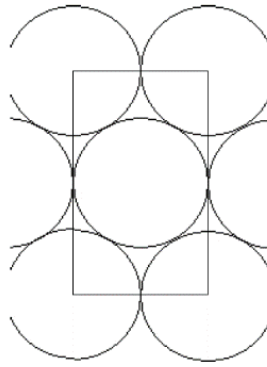


Figure 3.2 - Area box for the MRB wires.

As it can be seen, the area covered by the wires of diameter d_w inside the proposed area box is equivalent to two wires – one full wire and four quarters of a wire:

$$A_w = \pi \frac{d_w^2}{4} + 4 \times \frac{\pi}{4} \cdot \frac{d_w^2}{4} = \pi \frac{d_w^2}{2} \quad (45)$$

The height of the rectangle is estimated graphically to be $1.68d_w$. Thus, the area of the rectangular box shown in Figure 3.2 would be $1.68d_w^2$. Now, the total number of wire area boxes in the available coil area, $h_c(L - 2b_h)$, can be calculated by lower-rounding the following term:

$$N_b = \frac{h_c(L - 2b_h)}{1.68d_w^2} \quad (46)$$

The corresponding number of wire turns can then be predicted by the ratio of total area of the wires by area of one wire as:

$$N_c = \frac{N_b \times \pi d_w^2 / 2}{\pi d_w^2 / 4} = 2N_b \quad (47)$$

3.4. Finite Element Analysis of the MRB Magnetic Circuit:

To verify the analytical model obtained in the previous section, a Finite Element (FE) model has been developed using FEMM software which is an open source FE program (found on: <http://www.femm.info>) for solving low frequency two-dimensional and axisymmetric electromagnetic problems and steady-state heat transfer problems.

The 2D axisymmetric FEA model was developed inside the FEMM modeler workspace according to the geometric dimensions and specifications of the preliminary model provided in Table 3.1. Once the model is constructed, the material properties of different components are defined and assigned. Since the geometry is simple, the built-in automatic meshing tool in FEMM is utilized. Unstructured triangular mesh was created with 8103 nodes and 15844 elements with a precision of 1e-08. The resulting magnetic field density distribution under applied current of 2A is shown in Figure 3.3. It is noted that considering the available coil area in the initial design and wire Gauge-AWG 21 (diameter 0.7239 mm) and using Eq. (46) and Eq. (47) the number of coils is $N_c = 812$.

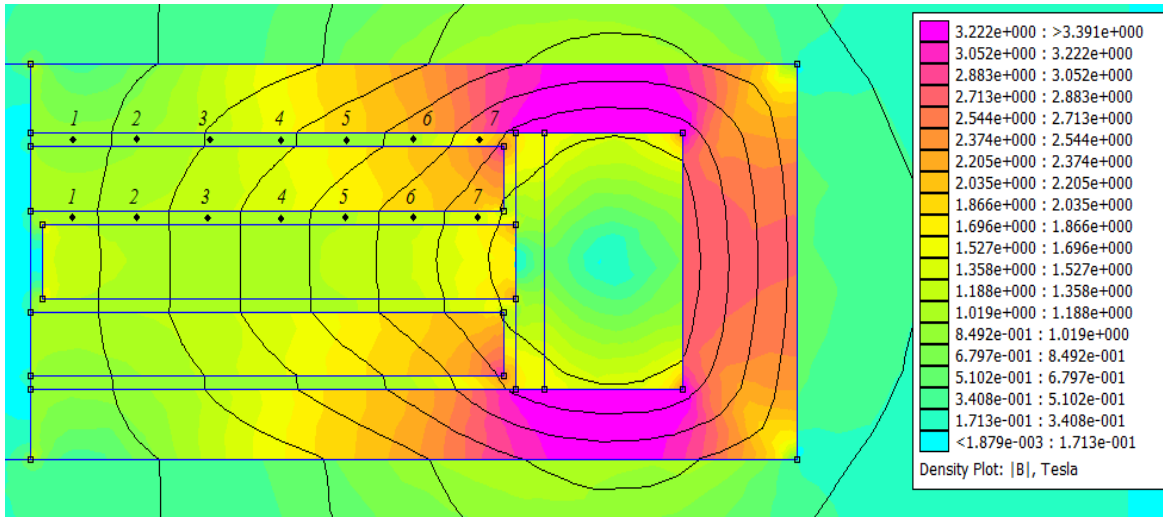


Figure 3.3 - Distribution of the magnetic flux density in the conventional MRB design using the FEMM software.

Examination of Figure 3.3 is required to calculate the average magnetic flux density in the MR fluid gap. Seven points were considered on both the outer and inner fluid gaps as shown in Figure 3.3. The values of magnetic flux density at each of the seven points for the outer and inner gaps are plotted in Figure 3.4 below.

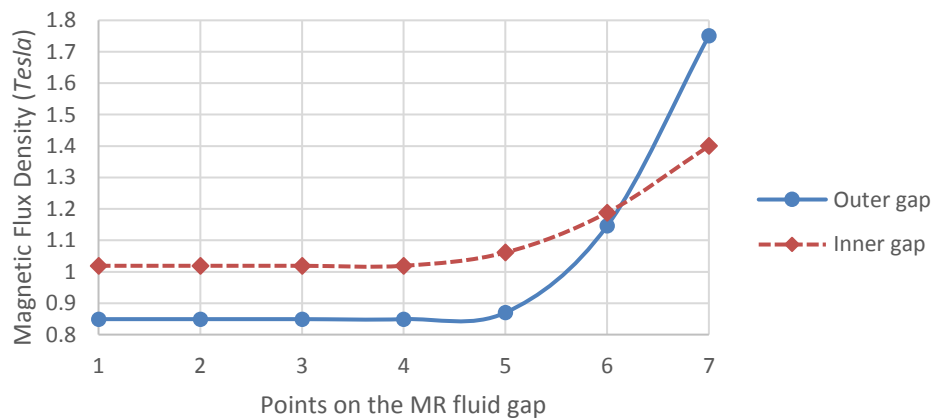


Figure 3.4 - The variation of flux density over the length of the MR fluid gap.

The average flux density over the fourteen considered points is calculated to be 1.02 *Tesla* on the outer fluid gap and 1.10 *Tesla* for the inner fluid gap. Thus, the average value for the magnetic field density along the shear gap region, according to the finite element analysis, is 1.06 *Tesla*.

Using the analytical model, the average magnetic flux density in the shear gap region of the MRB preliminary design is estimated to be 0.9929 *Tesla* which is reasonably close to that obtained using the finite element model. It should be noted that in the analytical model the relative permeability of the steel and MR fluid materials are considered to be constant; however, in reality, it varies as a function of magnetic flux density and temperature. Nevertheless, despite the assumption made on the relative permeability of steel and MR fluid - $\mu_s \approx 1000\mu_f$ - the numerical magnetic circuit model could provide fairly accurate results. Hence, the analytical model is validated.

3.5. Analytical Magneto-static Circuit Analysis - The decoupled MRB design:

For the proposed novel MRB design, a similar magnetic circuit formulation can be derived assuming perfect decoupling between MR fluids and the rotor in off-state configuration. The only difference would be replacing the term R_1 by R_2 . The effective lengths for the magnetic circuit in the proposed design as shown in Figure 2.7 are mostly the same as those of the conventional design, except for the 2nd and 12th members, which are expressed as:

$$l_2 = l_{12} = R - R_2 - \frac{g_a + t}{2} \quad (48)$$

where g_a is the length of the shear gap region as shown in Figure 3.5.

The links' corresponding cross-sectional areas for the proposed design are:

$$\begin{cases} A_1 = \pi[R^2 - (R-t)^2] \\ A_2 = A_{12} = \pi b_h(R-t+R_2) \\ A_3 = A_4 = \dots = A_{11} = \pi[R_0^2 - R_2^2] \end{cases} \quad (49)$$

Now, again, Eq. (44) can be utilized to estimate the average magnetic field intensity in the MR fluid region. Then using Eq. (19), the magnetic flux density can be evaluated.

In order to examine the ability of the permanent magnets in the current MRB design to completely pull the volume of the MRF into its adjacent gap, the Maxwell equation is adopted to define the permanent magnet's pull force. It is defined as:

$$F_{PM} = \frac{B_{PM}^2 A_{PM}}{2\mu_{sp}} \quad (50)$$

where B_{PM} is the magnetic flux density (*Tesla*) exerted by the permanent magnet, A_{PM} is the cross section area (m^2) of the of the pole and μ_{sp} is the permeability of free space. The magnetic flux density for a block type magnet is defined as [26]:

$$B_{PM} = \frac{B_r}{\pi} \left[\begin{array}{c} \arctan\left(\frac{L_m W}{2z\sqrt{4z^2 + L_m^2 + W^2}}\right) \\ - \arctan\left(\frac{L_m W}{2(D_m + z)\sqrt{4(D_m + z)^2 + L_m^2 + W^2}}\right) \end{array} \right] \quad (51)$$

where B_r is the remanence field of the permanent magnet – a property of the magnet that is independent of its geometrical dimensions. The permanent magnet chosen for this design is the Neodymium magnet N30EH since it is reputedly strong and operates at temperatures up to 200 °C. N30EH magnets are also known as neo rare earth magnets. They are composed of neodymium, iron and boron (NdFeB). For N30EH, B_r is between 1.08 to 1.13 *Tesla* [27]. The average value, 1.1 *Tesla*, is assumed for the current analysis. L_m , D_m and W are the length and thickness and width

of the block magnet, respectively. The width, W , of the PM in the current brake design is estimated as $W=2\pi R_e$. The parameter z is the distance of the attracted object from the pole face on the symmetry axis, as seen in the section drawing of Figure 3.5 below. The PM is desired to sufficiently pull the whole MR fluid volume. The maximum distance for z would be the distance from the face of the PM pole to the center of gravity, O_2 , of the MR fluid volume (on-state mode). It is expressed as:

$$z_m = d_f + \frac{g_a}{2} \quad (52)$$

In Figure 3.5, the cavity next to the permanent magnet is expected to hold the volume of the MR fluid. This geometric constraint allows the estimation of the required size of the corresponding cavity, d_f , as:

$$d_f = \frac{g_a d_c}{D_m} \quad (53)$$

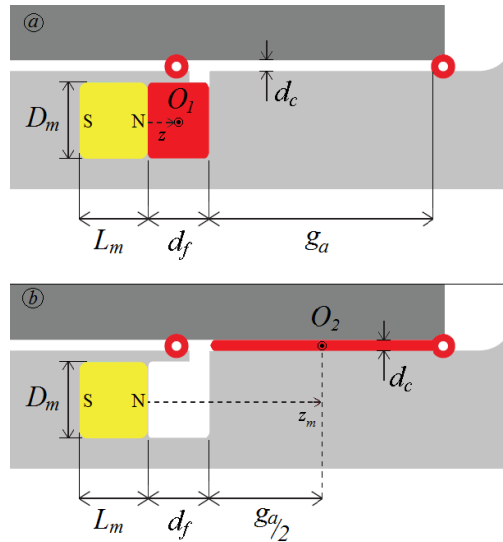


Figure 3.5 - Section sketch of the shear gap region the proposed MRB design in (a) OFF and (b) ON modes.

The forces acting on the MR fluid inside the MRB are the gravitational force, F_{gf} , due to the weight of the MR fluid, and the centrifugal force, F_{cf} , due to its rotation inside the MRB. A free body diagram (FBD) of the forces acting on an MR fluid particle is presented in Figure 3.6.

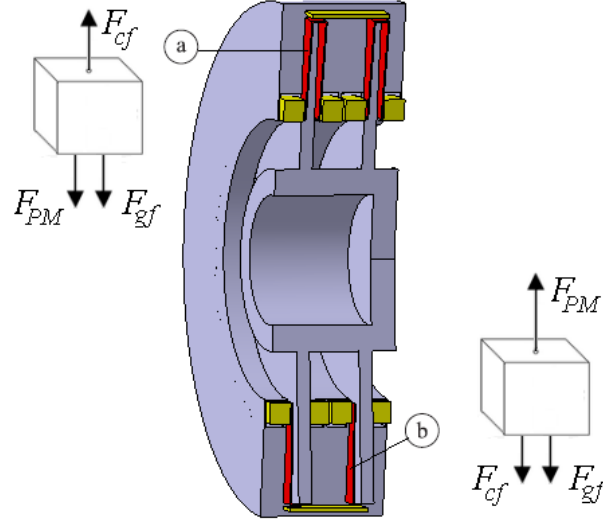


Figure 3.6 - FBD of MR fluid situated on (a) top end and (b) bottom end of the MRB.

In case (a), the MRF on the top of the brake are subject to a centrifugal force pushing it upwards while the forces from the PM and gravity are exerted downwards. In case (b) where the MRF is on the lower end of the brake, the centrifugal force would be pushing the fluid in the same direction as the gravitational force. The pull force of the PM has to be sufficient enough to attract the full amount of MRF into the cavity despite the two opposing forces. Hence, the condition for the pull force of the permanent magnet is represented as:

$$F_{PM} > F_{gf} + F_{cf} \quad (54)$$

which can be also written as:

$$\frac{B_{PM}^2 A_{PM}}{2\mu_{sp}} > m_f g + m_f \dot{\theta}^2 R_0 \quad (55)$$

where m_f and $\dot{\theta}$ are the MR fluid's mass and shaft's angular velocity, respectively. Thus, the minimum magnetic field density required by the permanent magnet to attract and fully pull the MR fluid can be calculated by:

$$B_{\min} = \sqrt{\frac{2\mu_{sp}m_f}{A_{PM}}(g + \dot{\theta}^2 R_0)} \quad (56)$$

Using the above formula, the proper permanent magnet with the required properties is selected and employed in the design. After this condition is met, to simplify the finite element analysis problem, it can be assumed that the transition between the “on” and the “off” state is instantaneous and the two cases are examined independently.

3.6. Temperature Build-Up-Heat Dissipation:

Two approaches are adopted to perform heat analysis in the MRB. For the vehicle's braking system, the kinetic energy due to the speed of rotation of the wheels is converted to thermal energy due to frictional stresses applied. Thus, due to the conservation of energy the heat generated (*Joules*) from braking is equal to the change in the kinetic energy as:

$$H_g = \Delta KE = \frac{1}{2} I_d (\dot{\theta}_i^2 - \dot{\theta}_f^2) \quad (57)$$

where $\dot{\theta}_i$ and $\dot{\theta}_f$ are the initial and final wheel angular speeds (*rad/s*) and I_d is the moment of inertia of the MRB disk(s), given by:

$$I_d = \frac{1}{2} m_t (R_1^2 + R_0^2) \quad (58)$$

with m_t being the equivalent load carried by each car wheel. Assuming an equivalent load of 455 *kg*, the moment of inertia of the preliminary MRB design is calculated to be 11.904 *kg.m²*.

Accordingly, the total heat generated from braking a vehicle at 70 km/hr ($\dot{\theta}_i = 59.69 \text{ rad/s}$) is calculated to be $21,209 \text{ Joules}$.

Gauss' Law states that the heat generation within a closed volume is equal to the heat flux out of the volume. The total heat generation is represented in the finite element model developed in FEMM software as heat flux boundary condition on each of the 8 MR fluid–steel contact surfaces with a magnitude equal to the total heat generated divided by eight. The results for the temperature distribution is shown in Figure 3.7 below.

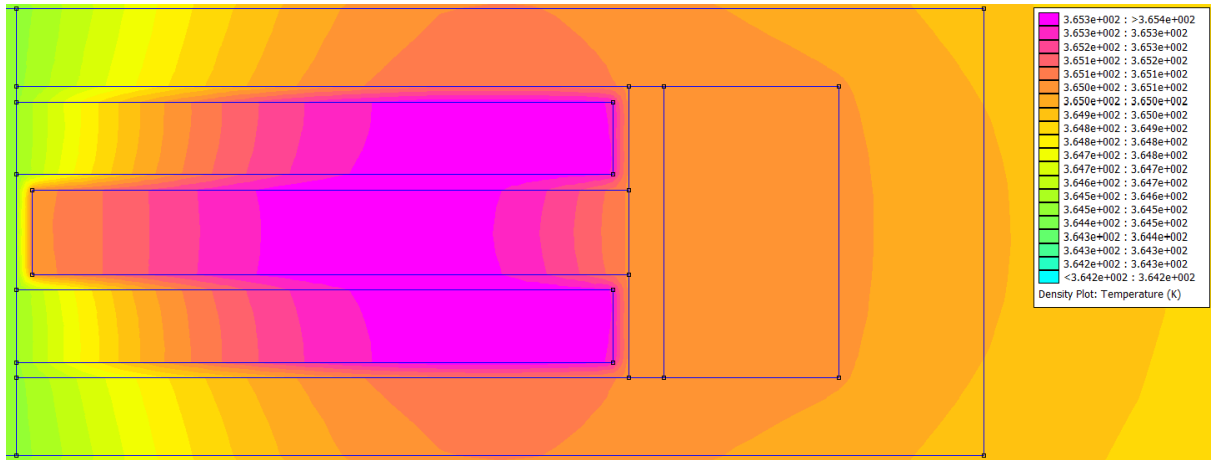


Figure 3.7 - Temperature distribution of the conventional MRB – Kinetic energy conversion.

After running the simulation, the maximum steady state temperature in the brake is found to be 365.3°K (92.3°C) which is less than the maximum operating point of MRF-132DG (130°C).

The second approach for heat analysis is based on the consideration of the friction on the contact surfaces. Frictional heat produced in the MRB will be absorbed partially by the disk and casing, and another part of the generated heat will be absorbed within the MR fluid. During

braking, when exposed to magnetic field, the MR fluid demonstrates a solid-like behavior. The activated MR fluid region is assumed to be a solid body which exerts a constant pressure equal to the shear stress, τ , on its surrounding surfaces. Thus, in this approach, the heat analysis is performed based on the conduction between two solid bodies. According to Ref. [28], the thermal contact is considered as one of two kinds: A *perfect contact*, where the surface temperature is considered equal between the two solid bodies, and an *imperfect contact*, which takes into consideration the thermal effects of the wear particles on the contact surface. For the MRB, there is no wear produced during braking. Thus, the contact between the MR fluid particles and the corresponding surrounding metal surface is considered to be a perfect contact. The amount of heat dissipated by each of the two bodies on one surface contact area is expressed by a partitioning factor, p_H [28]. For the steel-MRF contact, p_H is given by:

$$p_H = \frac{\xi_s}{\xi_s + \xi_f} \quad (59)$$

where ξ_s and ξ_f are the thermal effusivity properties of the steel and MR fluid component, respectively. The thermal effusivity is defined as [29]:

$$\xi = \sqrt{k\rho c} \quad (60)$$

where k is the heat conductivity (W/mC), ρ is the mass density (kg/m^3) and c is the specific heat (J/gC). The values of these parameters are tabulated in Table 3.2 for AISI 1018 steel and MRF-132DG.

Table 3.2 - Properties required to calculate the thermal effusivity.

	k (W/mC)	ρ (kg/m^3)	c (J/gC)
<i>AISI 1018</i>	<i>51.9</i>	<i>7.87×10^{-3}</i>	<i>0.486</i>
<i>MR-132DG</i>	<i>1.04</i>	<i>3.05×10^{-3}</i>	<i>$\sim 0.80^*$</i>

* The specific heat of MRF-132DG is not known so it was approximated to be equal to that of MRF-132AG.

The heat analysis and derivation for conventional brakes reported in [29] is adopted for the current MRB design. The rate of generated heat due to the shear stress between the two components at each surface of contact and at a radius, r , on the disk is equal to the friction power and is expressed as:

$$d\dot{E} = V \times dF_r = (r\dot{\theta})(\tau 2\pi r dr) \quad (61)$$

where V is the velocity and dF_r is the friction force at radius r on the disk. The total heat dissipated in the steel ($d\dot{E}_s$) and MR fluid ($d\dot{E}_f$) components for one contact surface are written as:

$$d\dot{E}_s = p_H \tau 2\pi \dot{\theta} r^2 dr \quad (62)$$

$$d\dot{E}_f = (1 - p_H) \tau 2\pi \dot{\theta} r^2 dr \quad (63)$$

The heat flux at the surface is obtained by dividing the rate of thermal energy by the surface contact area. The heat flux in the MR fluid section (*in W/m^2*) can be described as:

$$\ddot{q}_1(r, \dot{\theta}) = p_H r \dot{\theta} \frac{\tau(r, \dot{\theta})}{2} \quad (64)$$

Similarly, the heat flux in the steel sections is:

$$\ddot{q}_2(r, \dot{\theta}) = (1 - p_H) r \dot{\theta} \frac{\tau(r, \dot{\theta})}{2} \quad (65)$$

For the preliminary MRB design proposed, the partitioning factor, p_H , is equal to 0.8984. The heat flux in the MR fluid section is calculated to be 15,261 W/m^2 and the flux in the steel sections is found to be 1,550.2 W/m^2 . The heat flow problem is then simulated using FEMM software to find the temperature distribution in the MRB. The result for the temperature

distribution is shown in Figure 3.8. The maximum temperature inside the MR fluid is found to be 55.9°C which is significantly less than the upper limit operating temperature of MRF-132DG.

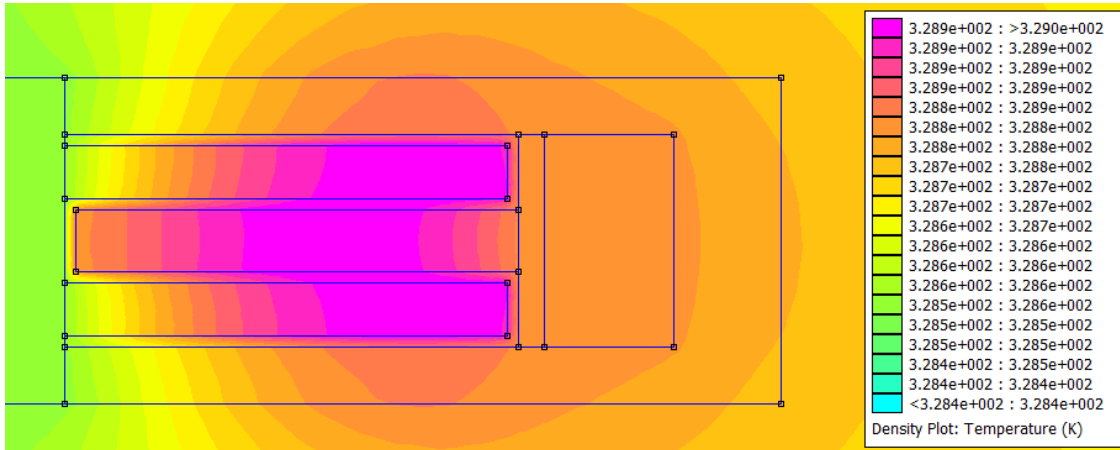


Figure 3.8 - Temperature distribution of the conventional MRB due to the shear stresses.

It is noted that the first method provides a higher steady state temperature value since it assumes that the kinetic energy is fully transferred to heat energy. In reality, energy is lost not only by heat or friction, but due to other forms of energy transfer like noise. The second method gives a low-temperature estimation because it strictly focuses on the heat generated due to surface friction between the MR fluid and the steel surfaces.

The proposed decoupled MRB design has a smaller shear gap region. Temperature generation due to shear stresses is less for the proposed design due to the smaller contact surfaces. Hence, the maximum reachable temperature is expected to be smaller than that of the conventional MRB design.

It is worthy to note that in the above heat transfer analysis, it is assumed that the vehicle stops under one single braking. In fact, repetitive braking cause continuous temperature build up in the MRB. Thus, further investigation through transient heat analysis would be required to model the temperature increase on multiple braking and to evaluate the limitations of the MRB design.

3.7. Summary:

Analysis of the MRB magnetic circuit led to the derivation of a relationship between the magnetic flux intensity as a function of applied current, number of coil turns and MRB geometric parameters. Magneto-static simulation on FEMM confirmed the results of the analytical model. Furthermore, heat analysis has been performed based on two approaches to calculate the maximum steady state temperature within the MRB configuration.

CHAPTER 4

DESIGN OPTIMIZATION OF THE MRB

4.1. Introduction:

In this chapter, a formal multidisciplinary design optimization including geometrical and magnetic circuit parameters will be formulated to improve the performance of the proposed MRB designs. The objective is to maximize the dynamic range and torque density while minimizing the electric power consumption and response time of the MRBs under geometrical, weight, magnetic field saturation limit, generated torque and viscous torque constraints. The stochastic based optimization method using genetic algorithm (GA) combined with gradient based mathematical programming technique using powerful sequential quadratic programming (SQP) technique has been implemented in the MATLAB environment to solve the formulated optimization problems.

4.2. The Performance Indices:

The optimal design of the MRB for vehicle application is formulated by maximizing the dynamic range and the torque density while minimizing the brake's power consumption and response time. The torque density (TD) is the ratio of total torque, T_b , to total volume, V_b , of the MRB, expressed as:

$$TD = \frac{T_b}{V_b} = \frac{T_b}{\pi R^2 L} \quad (66)$$

The electrical efficiency, EE , is another criterion to be taken into consideration in the optimization problem. It is defined as the ratio of the total torque capacity over power consumption (PC) of the electromagnet. It can be mathematically expressed as:

$$EE = \frac{T_b}{PC} = \frac{T_b}{i^2 R_{AWG}} \quad (67)$$

where i is the DC electric current supplied from the car battery and R_{AWG} is the electric resistance of the AWG21 wire, which can be calculated as follows [30]:

$$R_{AWG} = \frac{2\pi\bar{R}_w N_c r_{AWG}}{S_w} \quad (68)$$

with \bar{R}_w being the average radius of the coil from the center of the MRB, calculated as:

$$\bar{R}_w = R - t - \frac{hc}{2} \quad (69)$$

The term r_{AWG} is the resistivity of the AWG wire. In this study, the AWG21 is made of copper alloy with resistivity of 1.724×10^{-8} Ohms-m. S_w is the cross-sectional area of the AWG wires.

It is also intended to optimally design the MRB with improved response time. For an electric circuit with a resistor and an inductor, the inductive time constant is defined as the time required for the applied current passing through circuit wires to reach 63.2% of its maximum value. After five time constants, the electric current applied in the circuit reaches nearly 99.5% of its final value. A similar behavior also takes place when the current source is switched off. The relationship between applied current and inductive time constant, TC , is plotted in Fig. 4.1 below as the source is switched ON and OFF.

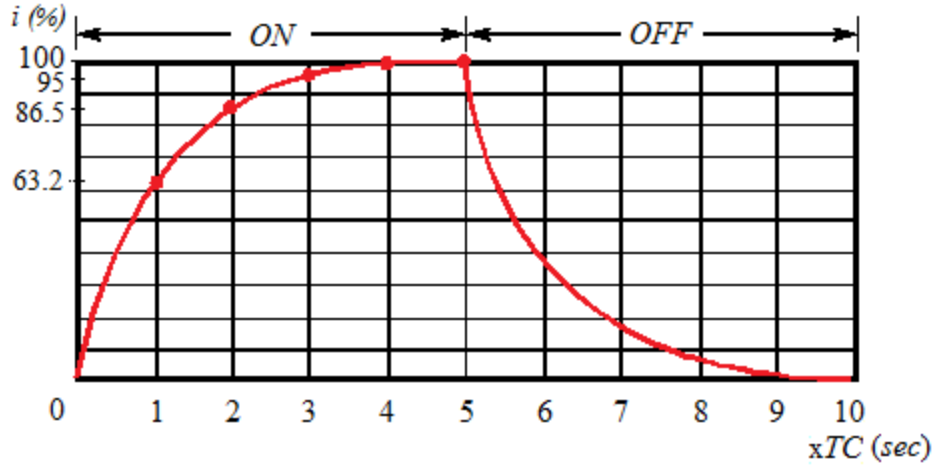


Figure 4.1 - Electric Current vs. Time Constant.

The lower is the inductive time constant, the faster is the response of the system. The inductive TC of the magnetic circuit of the MRB can be written as:

$$TC = \frac{L_{in}}{R_{AWG}} + t_e \quad (70)$$

where L_{in} is the inductance of the coil, calculated as:

$$L_{in} = \frac{N_c \Phi}{i} = \frac{N_c B A_c}{i} = \frac{N_c B \pi \bar{R}_w^2}{i} \quad (71)$$

and R_{AWG} is the resistance of the selected AWG wire defined in Eq. (68). The additional term, t_e , considers the additional time required by the MR fluid to activate and change its viscosity. For the conventional MRB design, the response time of the MR fluid to the applied magnetic field is less than 1 ms [11]. For the novel design with permanent magnet, the time required for the MR fluid to be transmitted to the shear gap region is adopted from [21] to be around 25 ms, delaying the total response time by 26 ms.

4.3. Multi-Disciplinary Optimization Problem:

4.3.1. The Conventional MRB Design

All significant geometrical parameters are considered as design variables. For the conventional 2-disk MRB design as shown in Figures 2.1, these include $R_1, R_d, c, d, d_c, d_0, d_i, h_c, t, b_h, b_d, b_c$. The optimization problem can be formally formulated as to find design variable vector:

$$X = [R_1, R_d, c, d, d_c, d_0, d_i, h_c, t, b_h, b_d, b_c]^T$$

to:

$$\text{Minimize } f(x) = \alpha_d \frac{DR_{ref}}{DR} + \alpha_t \frac{TD_{ref}}{TD} + \alpha_e \frac{EE_{ref}}{EE} + \alpha_s \frac{TC}{TC_{ref}}; \quad (72)$$

Subject to:

$$\text{Generated Torque: } T_b \geq 1010 \text{ Nm};$$

$$\text{Weight: } W_{MRB} \leq 60 \text{ kg};$$

$$\text{Volume: } L \leq 0.08 \text{ m}; \quad R \leq 0.2 \text{ m};$$

$$\text{Magnetic Field: } H \leq 300 \text{ kA/m}$$

$$\text{Side Constraints: } X_{\min} \leq X \leq X_{\max}$$

The variables α_d , α_t , α_e and α_s are weighting factors chosen for each of the four different performance measures. It is noted that the total sum of the weighting factors must be equal to 1. A reference value for each of the four specifications is assigned to achieve a dimensionless objective function. The chosen values for DR_{ref} , TD_{ref} , EE_{ref} and TC_{ref} are their upper bound values: 300, 200,000 N/m^2 , 30 $Nm/watt$ and 0.3 s , respectively. The side constraints on design variables are provided in Table 4.1.

Table 4.1 - Design variables and their ranges for the conventional MRB design.

<i>Design Variables</i>	<i>Geometric Ranges (cm)</i>
R_l	3.00 – 12.00
R_d	2.00 – 12.00
c	0.25 – 1.00
d	0.10 – 0.50
d_c	0.10 – 0.50
d_0	0.10 – 0.50
d_i	0.10 – 0.50
h_c	0.25 – 2.50
t	0.50 – 3.00
b_h	0.25 – 3.00
b_d	1.00 – 5.00
b_c	1.00 – 5.00

The weight constraint is set at 60 kg since it is almost equivalent to the weight of the conventional hydraulic brake system. W_{MRB} is calculated as a function of the brake's geometric dimensions. The procedure to evaluate W_{MRB} is provided in Appendix A. With respect to H , as the magnetic field increases, the magnetic material gets closer to its magnetic saturation limit and the ability to polarize it weakens. The saturation limit of MRF-132DG is obtained from its non-linear $B-H$ curve and is found to be 300kA/m. L and R are the total width and radius of the MRB, respectively. Their constraints are based on the available space inside the vehicle wheel. They are chosen in comparison with the conventional hydraulic brake dimensions.

4.3.2. The Novel Decoupled MRB Design

For the proposed MRB design shown in Figure 2.7, the geometrical parameters related to the permanent magnets and their gaps are also considered as design variables; in addition to the geometrical parameters of the conventional design. The design variable vector for the optimization of this design is:

$$X = [R_1, R_d, c, d, d_c, d_0, d_i, h_c, t, b_h, b_d, b_c, r_e, d_m, L_m]^T$$

It is noted that the variables r_e and d_m are used to calculate the effective radius of the permanent magnet, R_e , and the depth of the magnet, D_m , using the following relations:

$$R_e = R_1 + r_e R_d \quad (73)$$

$$D_m = d_m b_h \quad (74)$$

The objective function is similar to that defined in Eq. (72). However, since for the novel design there is no viscous torque, DR is equivalent to only T_b , and the reference dynamic range, DR_{ref} , is changed to T_{bref} with value of 1500 Nm.

$$\text{Minimize } f(x) = \alpha_d \frac{T_{bref}}{T_b} + \alpha_t \frac{TD_{ref}}{TD} + \alpha_e \frac{EE_{ref}}{EE} + \alpha_s \frac{TC}{TC_{ref}}; \quad (75)$$

Besides the constraints for conventional MRB discussed before, additional constraints are also added for the proposed design to ensure that the magnetic flux densities of the four permanent magnets satisfy the condition of being over the limiting value B_{min} given Eq. (56) that they would completely draw the full MRF volume to the gap region. Additional geometric constraints are added to restrict the MRB geometry from overlapping. In short, the new constraints are defined as:

$$B_{\min} \leq 4 B_{PM} \quad \frac{L_m}{2} \leq R_e - R_1 \quad b_c \geq 2b_h$$

The side constraints of the new design variables are provided below in Table 4.2.

Table 4.2 – New additional design variables and their ranges for the proposed MRB design.

<i>Design Variables</i>	<i>Geometric Ranges</i>
r_e (%)	10.0 – 90.0
d_m (%)	10.0 – 90.0
L_m (cm)	0.5 – 2.5

4.4. Multi-Objective Optimization Results:

The Genetic Algorithm toolbox in MATLAB environment is used to solve the optimization problems stated in Eq. (72) and Eq. (75). The Genetic Algorithm (GA) is a stochastic based optimization algorithm that is capable of capturing the near global optimum solution. GA mimics the natural evolution in which generations of improved chromosomes (design variables) are created by selection, mutation and crossover [25]. The fitness value (objective function) is evaluated for each generation and then, the best individuals are identified and chosen to build the next population. In the current study, the initial population size is chosen to be 150. At each generation, the top 5% chromosomes of the population pass directly as ‘Elite’ chromosomes to the following generation. For the remaining population, 80% undergoes crossover while the remaining part of the population undergoes ‘constraint dependent’ mutation before passing to the next generation. Iterations of this process are implemented until the average change in the objective function reaches the specified function (or constraint) tolerance of 10^{-6} . Additional stopping criteria are defined to stop the algorithm when the number of generations exceeds 1200 generation, or when 50 stall generations are passed.

For the first section of the study, it is desired to compare the two mathematical models - the Bingham and the Herschel-Bulkley models - for both the conventional and the proposed MRB designs. The four different performance indices used in the objective function are weighted

equivalently, i.e. with a weighting factor of 0.25 each. Optimal results for the MRB design parameters are provided in Table 4.3.

Table 4.3 - Genetic Algorithm Results – Design Parameters.

		Conventional		Novel	
		<i>Bingham</i>	<i>H. Bulk.</i>	<i>Bingham</i>	<i>H. Bulk.</i>
$f(x)$		1.1513	1.9037	2.4689	1.3946
<i>Iterations</i>		4	4	5	5
R_l	(<i>cm</i>)	9.88	3.01	9.65	7.86
R_d	(<i>cm</i>)	8.67	11.50	8.82	11.14
c	(<i>cm</i>)	0.25	0.25	0.27	0.25
d	(<i>cm</i>)	0.11	0.22	0.18	0.10
d_c	(<i>cm</i>)	0.10	0.23	0.10	0.18
d_0	(<i>cm</i>)	0.50	0.33	0.12	0.10
d_i	(<i>cm</i>)	0.50	0.31	0.50	0.50
h_c	(<i>cm</i>)	0.29	1.00	0.39	0.25
t	(<i>cm</i>)	0.50	0.50	0.59	0.50
b_h	(<i>cm</i>)	0.50	0.32	1.75	1.32
b_d	(<i>cm</i>)	1.00	1.00	1.04	1.00
b_c	(<i>cm</i>)	1.01	1.00	3.50	2.55
r_e	(%)	-	-	30.73	28.19
d_m	(%)	-	-	90.00	90.00
L_m	(<i>cm</i>)	-	-	4.14	6.14

It can be seen that for both the conventional and the novel design, the chosen values for R_l are larger in the Bingham model while the values for R_d were higher for the Herschel-Bulkley model. This indicates that the MRB designs based on the Bingham model can reach the required braking torque with a smaller shear gap region. In other words, the Bingham model might be falsely estimating the braking torque. For the purpose of comparing the accuracy of the adopted mathematical models, the optimal parameters based on Bingham model for the conventional MRB design are used for design based on the Herschel-Bulkley model, and vice versa. The geometric

and performance measures resulting from the optimal design parameters of Table 4.4 are tabulated below.

Table 4.4 - Genetic Algorithm Results – MRB Characteristics.

<i>Model</i>		Conventional				Novel	
		<i>Bingham</i>		<i>H. Bulk.</i>		<i>Bingham</i>	<i>H. Bulk.</i>
<i>on equations of:</i>		<i>B.</i>	<i>H.B.</i>	<i>B.</i>	<i>H.B.</i>	<i>B.</i>	<i>H.B.</i>
<i>DR</i>	-	638.65	58.57	859.80	176.64	-	-
<i>TD</i>	(<i>N/m²</i>)	179,010	363,860	217,910	334,880	84,667	141,760
<i>EE</i>	(<i>Nm/watt</i>)	21.93	44.57	5.90	9.07	9.36	23.51
<i>TC</i>	(<i>ms</i>)	498.4	498.4	603.4	603.4	847.2	545.4
<i>T_b</i>	(<i>Nm</i>)	1,005.5	2043.9	858.24	1,318.9	1,010	1,397.6
<i>T_{vis}</i>	(<i>Nm</i>)	1.57	34.89	1.00	7.47	-	-
<i>W_{MRB}</i>	(<i>kg</i>)	29.44	29.44	25.59	25.59	39.94	34.16
<i>R</i>	(<i>cm</i>)	20.00	20.00	16.59	16.59	19.83	20.10
<i>L</i>	(<i>cm</i>)	4.43	4.43	4.55	4.55	9.66	7.77
<i>B_{min}</i>	(<i>Tesla</i>)	-	-	-	-	0.1096	0.1796
<i>B_{PM}</i>	(<i>Tesla</i>)	-	-	-	-	0.4194	0.4289

Examination of Table 4.4 reveals that the Bingham model underestimates both the braking torque capacity and the viscous torque generation, which leads to an overestimation of the MRB's dynamic range to up to 10 times that of the Herschel-Bulkley model. The torque density is also underestimated while all the other properties remain unaffected. The inaccuracy of the Bingham model is due to the assumption made on the parameter μ_0 (See Eq. (8) in Chapter 2) that it is constant and independent of the magnetic field. In fact, this parameter is expected to increase with the increase in magnetic field, similarly to the parameters K and n of the Herschel Bulkley model. Hence, the Herschel Bulkley model is selected to model the proposed MRB designs.

The Genetic Algorithm reached a minimum point of the objective function that satisfies the defined constraints. This point is given the term 'Global' optimum point. For both chosen MRB

designs, the braking torque capacity was almost equivalent to 1,300 *Nm*. The novel MRB design had the advantage of having a higher electric efficiency with a lower response time and zero viscous torque. On the other hand, the conventional MRB design displayed higher torque density while having a uniquely low weight. To confirm the accuracy of the global minimum point of the Genetic Algorithm, Sequential Quadratic Algorithm (SQP), which is a powerful gradient based optimization algorithm capable of catching ‘Local’ optimum solutions, was utilized. The SQP algorithm requires an initial point from which it starts its first iteration and stops when the objective function reaches the closest minimum. The global optimum parameters obtained from the GA optimization are taken as the initial point for the SQP algorithm. The resulting optimal design is given the term ‘True Global’ optimum. The resulting geometric variable and design parameters are tabulated in Table 4.5.

Another investigation on the selection of the weighting factors is performed to search for the absolute minimum. The weighting factors are inputted as design variables ranging from 0 to 1. An additional equality constraint is added to restraint the sum of weighting factors to 1. This optimization varies the distribution of weighting factors to find an even lower value for the objective function, given the term ‘Absolute Global’ optimum. The combined GA-SQP optimization method is utilized for this optimization problem and the resulting MRB characteristics are presented in Table 4.5.

Table 4.5 - True and Absolute Global Optimization Results using combined GA and SQP.

		True Global Optimum		Absolute Global Optimum	
		<i>Conventional</i>	<i>Novel</i>	<i>Conventional</i>	<i>Novel</i>
$f(x)$		1.6562	1.2403	0.7755	0.6460
<i>Iterations</i>		9	8	9	11
R_l	(cm)	4.31	6.69	3.00	7.02
R_d	(cm)	10.67	12.00	11.65	11.88
c	(cm)	0.20	0.25	0.25	0.25
d	(cm)	0.10	0.10	0.50	0.10
d_c	(cm)	0.10	0.10	0.50	0.10
d_o	(cm)	0.46	0.10	0.50	0.10
d_i	(cm)	0.47	0.11	0.50	0.10
h_c	(cm)	0.32	0.25	1.00	0.25
t	(cm)	0.60	0.50	0.50	0.50
b_h	(cm)	0.90	1.37	0.25	1.90
b_d	(cm)	1.00	1.00	1.00	1.00
b_c	(cm)	1.00	2.74	1.00	3.80
r_e	(%)	-	29.75	-	26.18
d_m	(%)	-	89.78	-	90.00
L_m	(cm)	-	6.31	-	5.38
<i>MRB Specs</i>					
DR	-	94.19	-	262.34	-
TD	(N/m^2)	221,400	185,090	205,400	178,970
EE	(Nm/watt)	23.51	30.99	5.34	31.32
TC	(ms)	378.2	628.2	471.1	726.1
T_b	(Nm)	1,043.8	1,832.9	1,013.8	2,249.1
T_{vis}	(Nm)	11.08	0	3.864	0
W_{MRB}	(kg)	30.50	38.71	28.89	53.61
R	(cm)	16.61	20.00	16.90	20.00
L	(cm)	5.44	7.88	5.50	10.00
B_{min}	(Tesla)	-	0.1801	-	0.3155
B_{PM}	(Tesla)	-	0.3511	-	0.3155
<i>Weighting Factors</i>					
α_d	(%)	25	25	66.67	100.00
α_t	(%)	25	25	0	0.00
α_e	(%)	25	25	0	0.00
α_s	(%)	25	25	33.33	0.00

The objective function using combined GA and SQP is nearly 12% less than that using GA alone for both MRB designs. However, at the absolute optimal point, the value of the objective function is further reduced to nearly half of its value at the true optimal.

At the absolute optimum, the conventional MRB design had an upper bound value of 0.5 *cm* for its parameters d , d_c , d_0 and d_i . This large value is selected by the optimization program to reduce the viscous torque generation. Nevertheless, according to Eq. (4), as the thickness of the shear gap region increases, the shear rate decreases. Torque generation is not effective at low shear rates (See Figure 2.5). As a result, the conventional design required a larger h_c , which means more wire turns for the brake's electromagnet, to reach the braking capacity of 1013.8 *Nm*. Overall, the conventional design demonstrated a dynamic range of 262 while having 40% faster response time and being nearly 50% lighter than the novel design. Nonetheless, despite the impressive specifications of the conventional MRB design, the novel MRB design is favored for its complete elimination of the viscous torque. Furthermore, the novel design reached more than double the braking torque capacity and more than 4 times the electrical efficiency.

4.5. Additional investigation on weighting factors distribution:

In Table 4.5, the selected distribution of the weighting factors indicates that the most dominant weighting factor is that of the dynamic range. It was given the values 66.67% for the conventional and a full 100% for the novel MRB design. Another important performance index for the application of MRB in a real-vehicle is its response time. Typically, giving the inductive time constant a small weighting factor does not match the design requirements for automotive applications. The achieved torque capacity is twice as much as the minimum required value while the time constant is more than twice of the reference value. Thus, further investigation is required

to find the most efficient MRB design for application in real vehicles. Thus, here for the novel design, the weighting factors, α_t and α_e , of the *TD* and *EE* are equated to zero, while the weighting factors, α_d and α_s , of *DR* and *TC* are varied in increments of 0.1. The combined GA-SQP optimization method is then performed on each step. The variation of the optimal objective function versus the weight factor α_d for braking torque is shown in Figure 4.2.

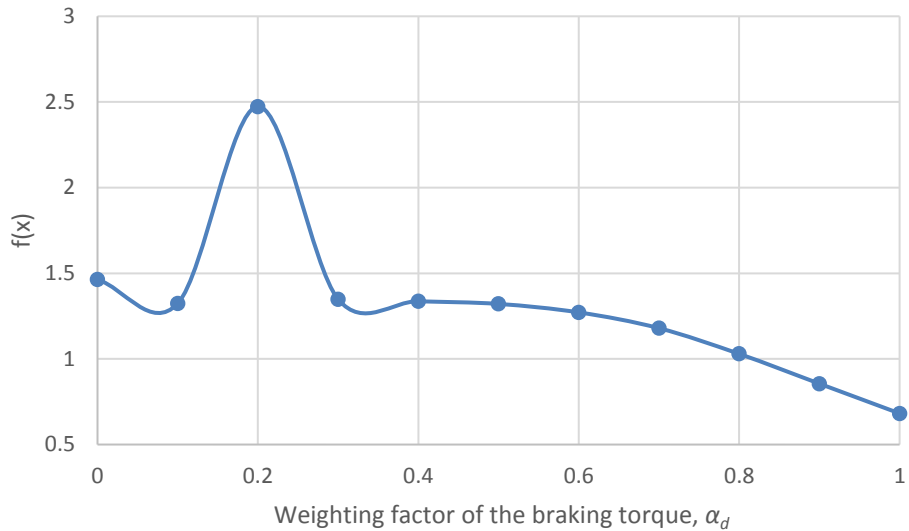


Figure 4.2 - Change of objective function as a function of weighting factor.

Figure 4.2 shows that the absolute minimum of the objective function is reached at $\alpha_d = 1$; confirming the results in Table 4.5. Examination of Figure 4.2 also reveals that the optimal objective function reaches to maximum value of 2.5 at $\alpha_d = 0.2$. To further investigate this, the optimization is run again between values of α_d ranging from 0.1 to 0.3 in increments of 0.025. The value of optimal objective function achieved at each step is then recorded and shown in Figure 4.3.

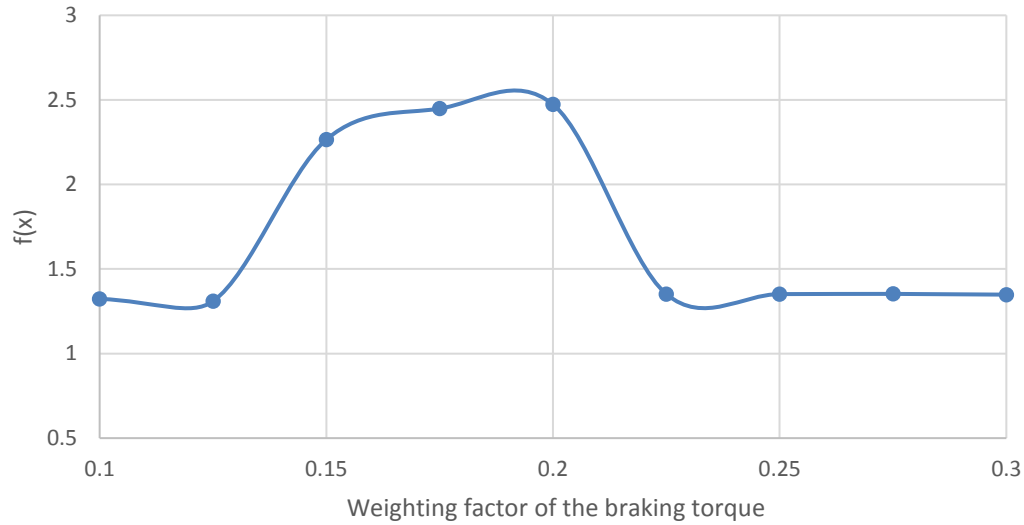


Figure 4.3 - Zoomed resolution of the objective function value over the weighting interval.

Figure 4.3 confirms that there is an increasing trend within the selected interval. The values of the optimal function at weight factors $\alpha_d = 0.15, 0.175$ and 0.2 were close to 2.5 while those for all other weighting factors were below 1.5 . The main performance measures of the resulting designs are also recorded at each increment and plotted in Figure 4.4 as ratios of their values at the specific design point over their reference values. As mentioned before the reference values for braking torque (T_{bref}), torque density (TD_{ref}), electrical efficiency (EE_{ref}) and time constant (TC_{ref}) are 1500 N.m , $200,000 \text{ N/m}^2$, 30 Nm/watt and 0.3 s , respectively. The reference value for MRB weight, W_{ref} , is chosen to be 40 kg .

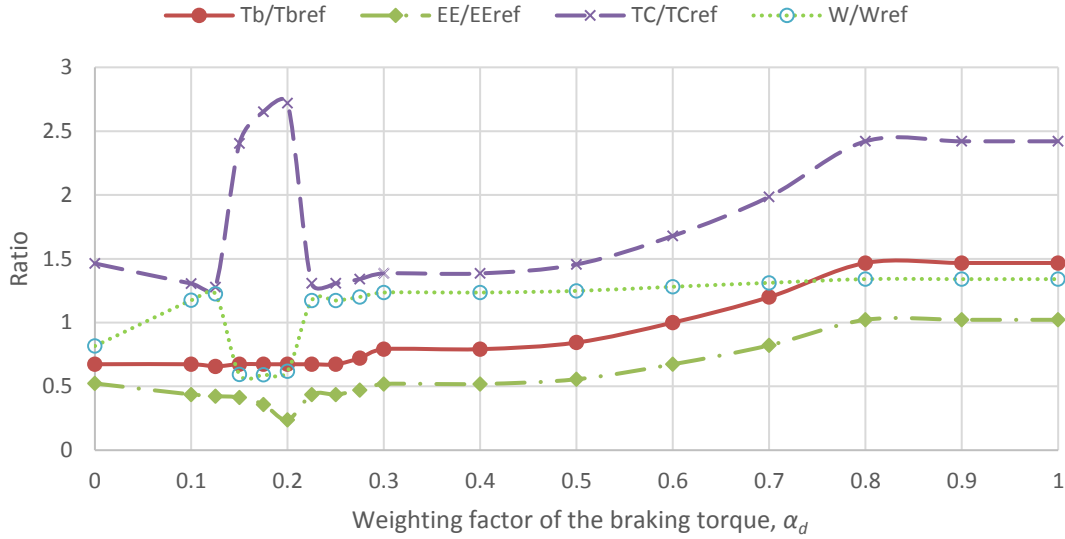


Figure 4.4 - MRB performance specs versus maximum torque weighting factor.

It can be seen from Fig. 4.4 that as α_d increases, the braking torque capacity continuously increases. The brake's inductive time constant follows an unstable trend. The time constant ratio starts at 1.5, decreases to around 1.3 at $\alpha_d = 0.1$, peaks to 2.7 ($TC=816\text{ ms}$) at $\alpha_d = 0.2$, falls back to 1.4 at the next iteration, then continuously increase for the following iterations saturating at nearly 2.5 at the final three steps. The variation of TC as a function of braking torque capacity for the continuously increasing region ($\alpha_d = 0.3-0.8$) is shown in Fig. 4.5. The electrical efficiency decreases to around 0.25 (7 Nm/watt) at $\alpha_d = 0.2$ after which it follows an increasing trend that reaches to its reference value of 30 Nm/watt at the final three iterations. As for the MRB weight, it increases from 33 kg at $\alpha_d=0$ to 47 kg after the first iteration, then reduces to 25 kg at the second iteration before it steadily increases to around 55 kg at $\alpha_d = 1$.

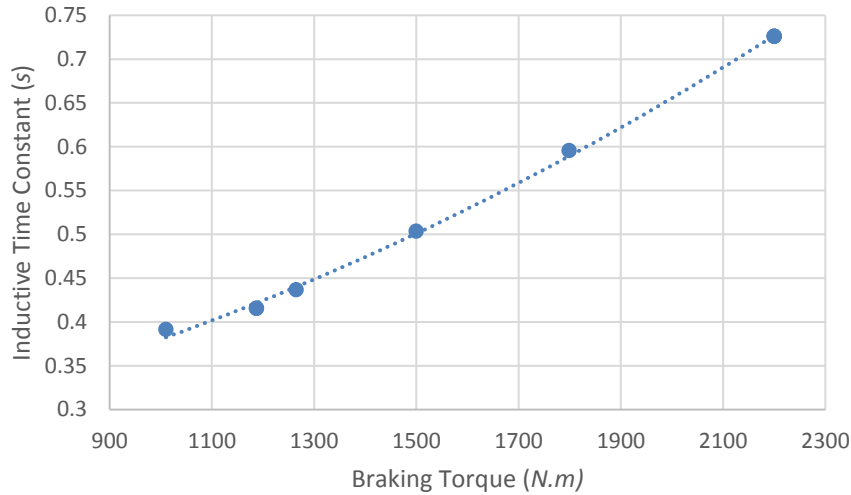


Figure 4.5 - TC versus T_b for the different design points.

The drawback to the optimal MRB designs is their time response. The inductive time constants for the proposed MRB designs are ranging from 401 ms to 816 ms . This value is exceedingly high compared with that of conventional hydraulic braking systems, which demonstrate a full response time (equivalence of $5TC$) of 300 ms . The inductive time constant is inversely proportional to the resistance of its electric circuit. A suggestion to decrease the response time of the brake is to increase the equivalent resistance of the circuit by adding a resistor in series to the car battery – MRB electric circuit. Knowing that after $3TC$, the applied current is at 95% of its final value, a constraint is formed to equate the required response time, $3TC$, to 300 ms , making:

$$TC = t_e + \frac{L_{in}}{R_{AWG} + R_{es}} = 100ms \quad (76)$$

where R_{es} is the required resistance ($Ohms$) to be added to the car battery-MRB electric circuit in series, as shown in the figure below.

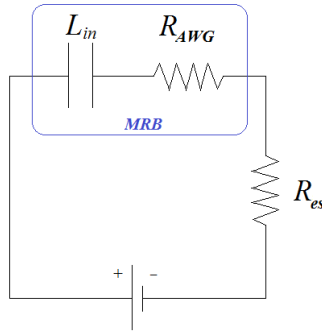


Figure 4.6 - Addition of R_{es} to the car battery – MRB electric circuit.

Rearranging Eq. (76) allows the estimation of R_{es} for the different designs obtained in the previous section.

$$R_{es} = \frac{L_{in}}{100ms - t_e} - R_{AWG} \quad (77)$$

Adding a resistor to the circuit has the disadvantage of increasing its power consumption. Different types of resistors can be added to reduce the time response, but it would contribute to an increase in the MRB design's power consumption. The plot in Fig. 4.7 shows the variation of power consumption as a function of desired time constant at different electric circuit design options. Adding a resistor to the circuit can effectively reduce its response time. As the resistance is increased, the power consumption exponentially increase. For example, the addition of a 30 *Ohms* resistor results in a *TC* of 300 *ms* with no significant change in power consumption. On the other hand, adding a 600 *Ohms* resistor reduces the *TC* to 50 *ms*, but largely contributes to the brake's power efficiency, as seen in Fig. 4.7.

A 200 *Ohms* resistor is chosen to be added to the electric circuit of the final MRB design. The resulting inductive time constant is 85.3 *ms* and having a power consumption, at maximum braking, of 871 *watts*, which is equivalent to 1.17 *hp*.

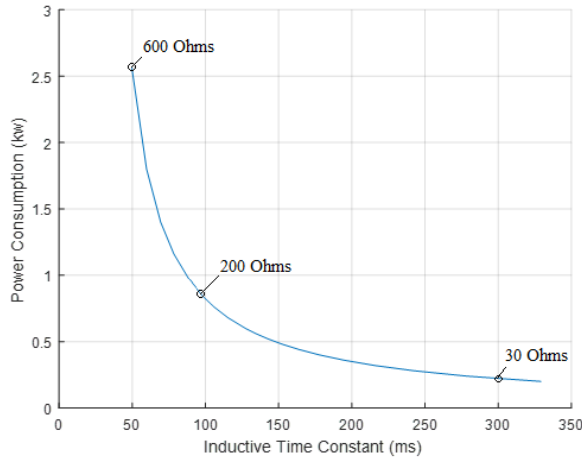


Figure 4.7 - Variation of *PC* versus *TC* for different *Res*.

The geometry and specifications of the final MRB design are summarized below.

Table 4.6 - Geometric variables and specifications for the selected optimal MRB design.

MRB Geometry			MRB Specs		
R_l	(<i>cm</i>)	7.02	TD	(N/m^2)	178,970
R_d	(<i>cm</i>)	11.88	EE	($Nm/watt$)	2.58
c	(<i>cm</i>)	0.25	PC	(<i>watts</i>)	871.80
d	(<i>cm</i>)	0.10	TC	(<i>ms</i>)	83.7
d_c	(<i>cm</i>)	0.10	R_{es}	(<i>Ohms</i>)	200
d_0	(<i>cm</i>)	0.10	T_b	(Nm)	2,249.1
d_i	(<i>cm</i>)	0.10	T_{vis}	(Nm)	0
h_c	(<i>cm</i>)	0.25	W_{MRB}	(<i>kg</i>)	53.61
t	(<i>cm</i>)	0.50	R_2	(<i>cm</i>)	12.96
b_h	(<i>cm</i>)	1.90	R	(<i>cm</i>)	20.00
b_d	(<i>cm</i>)	1.00	L	(<i>cm</i>)	10.00
b_c	(<i>cm</i>)	3.80	B_{min}	(<i>Tesla</i>)	0.3155
R_e	(<i>cm</i>)	10.13	B_{PM}	(<i>Tesla</i>)	0.3155
D_m	(<i>cm</i>)	1.71	H	(kA/m)	112.10
L_m	(<i>cm</i>)	5.38	N_c	(<i>turns</i>)	352

4.7. CAD Model of the Optimal Proposed Design:

Using the final optimal dimensions presented in Table 4.6, a CAD model of the optimal configuration of the proposed novel design has been constructed in CATIA. A section representation of the CAD model is shown in Figure 4.8. The detailed CATIA drawing with relative dimensions is presented in Appendix B.

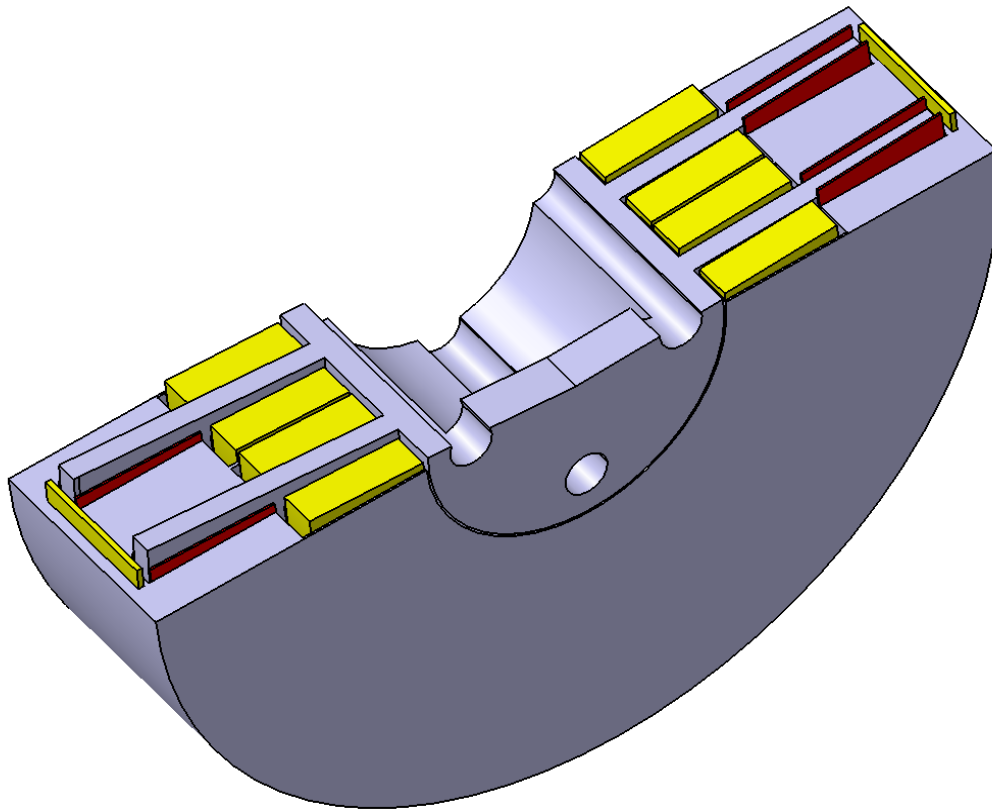


Figure 4.8 – CAD model of the optimal configuration of the proposed MRB.

4.8. Summary:

After defining the main MRB specifications, GA optimization has been performed on the two proposed designs modeled by each of the two mathematical models. The Herschel-Bulkley model was preferred to model the MRB since the Bingham model proved to give underestimated

values for the MRB's torque generation. The SQP algorithm combined with GA and considering variable weighting factors proved to reduce the minimum value for the objective function to approximately 44% compared with that based on GA alone. In conclusion, the novel MRB design demonstrated better specifications for automotive applications by its massive braking torque and zero viscous torque. Further fine tuning of the novel design's magnetic circuit (the addition of a 200 Ohm resistor) allowed the reduction of the response time by nearly 90% while maintaining reasonable power consumption.

CHAPTER 5

APPLICATION OF MRB IN REAL-SIZE VEHICLE

5.1. Introduction:

It is essential for the vehicle to be designed with brakes that offer a decent stopping time with a smooth deceleration. This chapter serves to provide a real-vehicle application for the selected optimal MRB designs. It is required to investigate the behavior and ensure an accurate characterization and optimization of the real-vehicle MRB designs.

5.2. Vehicle Dynamic Model:

The quarter vehicle model is used to simplify the vehicle system. This model assumes that each wheel of the vehicle carries identically the same load, which is quarter of the vehicle mass. Let us consider the braking of a wheel of radius R_w rotating clockwise, with applied braking torque of T_b as shown in Figure 5.1. The forces acting on the wheel during braking are the normal force (F_n), rolling resistance force (F_r), friction force (F_f), weight and force of transferred weight due to braking (F_L). The free body diagram representing the vehicle wheel is schemed in Fig. 5.1.

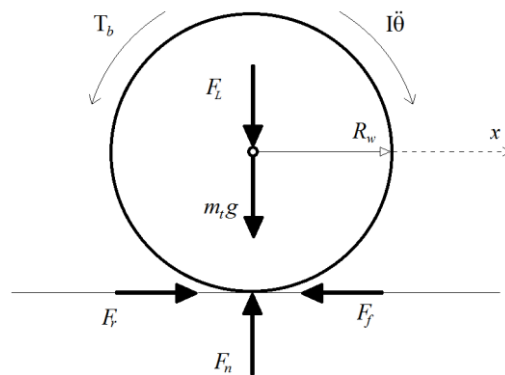


Figure 5.1 - Vehicle Wheel – Free body diagram.

It is note that in the Figure 5.1, m_i is the total load mass carried by the wheel. For the quarter model, the total load is:

$$m_t = \frac{1}{4}m_v + m_w \quad (78)$$

where m_v is the vehicle mass and m_w is the wheel mass. $\ddot{\theta}$ is the angular acceleration of the wheel and I is the effective moment of inertia defined as:

$$I = I_w + \frac{1}{2}\varphi^2 I_e + I_y \quad (79)$$

I_w and I_e are the inertia of the wheel and engine respectively, φ is the gear ratio, and I_y is the total inertia of the brake discs. The term $\varphi^2 I_e$ is divided by two taking into account that the engine inertia is distributed between the two driving wheels. The force of rolling resistance is defined by [31] as:

$$F_r = f_0 + 3.24f_s \left(K_v \frac{\dot{x}}{100}\right)^{2.5} \quad (80)$$

where K_v is the speed conversion factor from m/s to mph , 2.237, and f_s and f_0 are curve fit parameters. The friction force acting on the wheel is a function of the normal force, expressed as:

$$F_f = \mu F_n \quad (81)$$

$$F_n = m_t g + F_L \quad (82)$$

$$\text{with } F_L = \frac{m_v h_{CG}}{l_{base}} \ddot{x} \quad (83)$$

where h_{CG} is the height of the center of gravity and l_{base} is the wheel base. μ is the friction coefficient and is a function of the slip ratio, s_r , which is the rolling to slipping proportion, defined as:

$$s_r = \frac{\dot{x} - R_w \dot{\theta}}{\dot{x}} \quad (84)$$

Here, $\dot{\theta}$ is the angular velocity of the wheel. The relation between μ and s_r depends on the interacting surface. Figure 5.2 below presents the correlation between friction coefficient and slip ratio for dry, wet, snowy, and icy roads [32].

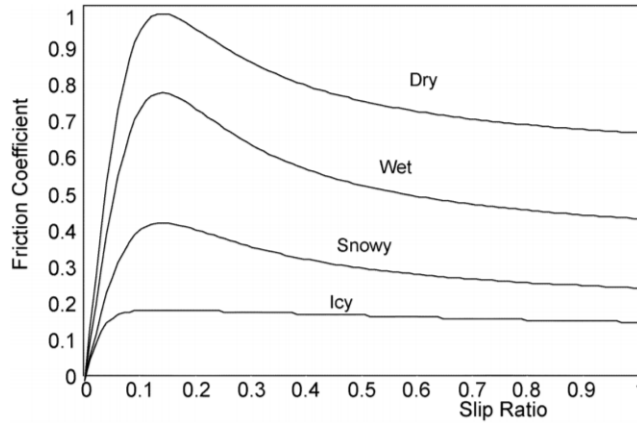


Figure 5.2 - Friction Coefficient as a function of different road surfaces [32].

Applying Newton's law on the quarter vehicle model, the equations describing the motion of the wheel can be written as:

$$m_t \ddot{x} = F_r - F_f \quad (85)$$

$$I \ddot{\theta} = -T_b + R_w F_f - R_w F_r \quad (86)$$

The preceding equations are the force equilibrium equation in the direction of motion and the moment equilibrium equation around the axis of the wheel. Solving this system of equation yields the calculation of the required braking torque to stop the vehicle. To represent the vehicle model, some physical parameters should be given. These parameters are adopted from [5] and [33] and tabulated below in Table 5.1.

Table 5.1 - Parameters for the quarter car model with MRB.

R_w	<i>Wheel Radius</i>	<i>0.326 m</i>
l_{base}	<i>Wheel Base</i>	<i>2.5 m</i>
h_{CG}	<i>Center of Gravity Height</i>	<i>0.5 m</i>
m_w	<i>Wheel Mass</i>	<i>40 kg</i>
$m_w/4$	<i>Quarter of the Vehicle Mass</i>	<i>415 kg</i>
I_t	<i>Total Moment of Inertia of Wheel and Engine</i>	<i>1.75 kg.m²</i>
f_o	<i>Basic Coefficient</i>	<i>10e-2</i>
f_s	<i>Speed Effect Coefficient</i>	<i>0.005</i>

5.3. MRB Control:

The main advantage of the Magneto-Rheological Brake compared with convectional MRB is that it can be semi-actively controlled and operates on electric current. This makes the brake control easy and rapid through an electronic system. The control system can easily be adjusted or upgraded to optimize stability and stopping time whilst regulating the slip ratio and preventing wheel lockup [5]. The control system can be achieved by modelling the vehicle dynamics of the system into a plant and designing a suitable controller.

5.3.1. MRB-Vehicle Plant:

The focal objective of the controller presented in this project is to minimize the braking time through maintaining the desired slip ratio. It is required to formulate a plant to describe the dynamics of the MRB-vehicle system. The equations of motion of the vehicle model can be rearranged as:

$$\ddot{x} = \frac{F_r - \mu F_n}{m_t} \quad (87)$$

$$\ddot{\theta} = -\tau_b + \mu \tau_n - \tau_r \quad (88)$$

where:

$$\tau_b = \frac{T_b(i, \dot{\theta})}{I} = \frac{T_H(H) + T_\mu(\dot{\theta})}{I} \quad (89)$$

$$\tau_n = \frac{R_w F_n}{I} \quad (90)$$

$$\tau_r = \frac{R_w F_r}{I} \quad (91)$$

T_H is a function of magnetic field density, which is a function of electric current, and T_μ is a function of the rotational speed of the wheel. A SIMULINK model has been constructed in the MATLAB environment to describe and solve the MRB-vehicle plant as shown in Figure 5.3.

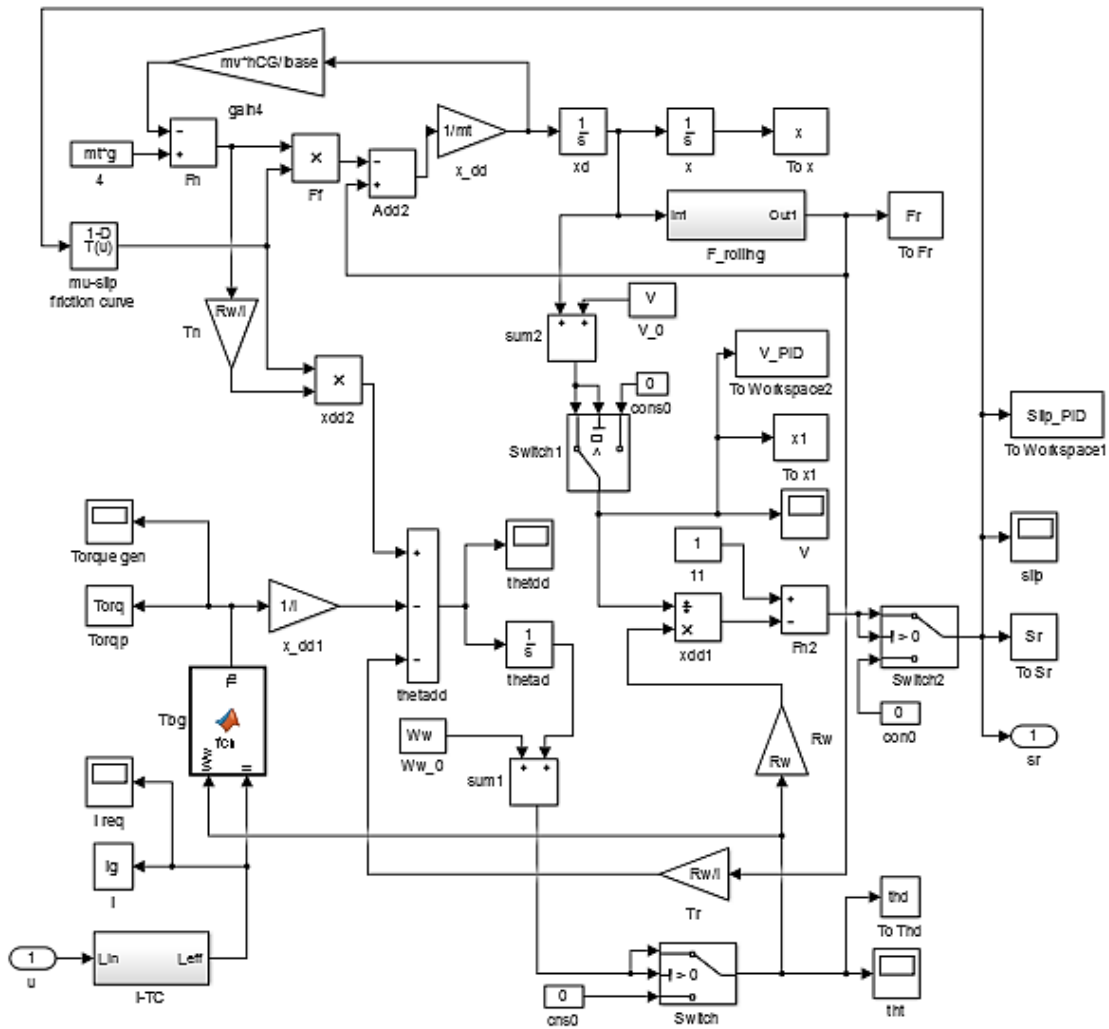


Figure 5.3 - SIMULINK model of MRB-vehicle plant.

The control input of the MRB-vehicle plant is electric current, shown in Fig. 5.3 as block “*u*.” The time response property of the MRB’s electromagnet is modeled by a subsystem, block “*i_TC*,” that estimates the equivalence of effective current that is capable of creating the desired magnetic field within the MRB. The effective current is fed into a *MATLAB* user-defined function that calculates the total braking torque depending on inputted current and the wheel’s rotational speed. The calculated braking torque is then utilized in the equations of motion to calculate the new rotational (wheel) and vehicle speed. The preceding values are finally employed to estimate the sliding ratio, which is the output of the MRB-vehicle plant.

Since the dynamic vehicle model of the MRB is nonlinear and time-variant, basic controller design methods cannot be implemented. The implementation of nonlinear techniques, like the phase plane method and the describing function method is generally avoided due to its complexity since there is no general or simple design method to refer to all nonlinear control system [34]. Linearization of the plant at hand and utilizing linear design schemes may not be favored as the resulting system cannot be guaranteed to be satisfactory. It would require several adjustments in the compensator parameters in hope of finding the satisfactory model.

In the present study, a proportional-integral-derivative (PID) controller has been utilized. The PID controller might require the modification of its parameters, however this can be easily achieved by the trial and error to find the final most suitable system. PID controllers are common products in the market and broadly employed in different industries.

5.3.2. PID Configurations:

Some industrial plants apply controllers in an open loop configuration as shown in Figure 5.4 (a). This is common when the plant and the controller are stable. However, the addition of a feedback is desired in control systems because it improves the performance of the system and eliminates the need to readjust any controller parameter, which is the case for open loop configurations. This is the most common configuration for PID and, thus, given the name "textbook PID controller" [34] is shown in Figure 5.4 (b). For systems that have a variable and discontinuous reference input, different types of PID controllers are utilized to avoid the generation of large actuating error signals. One type, called "derivative-of-output controller" [34] is shown in Fig. 5.4 (c). Here, the error signal would pass in u but would not be amplified by differentiation. Another approach is proposed to smoothen the discontinuity of the input signal by integration only. This configuration is shown in Fig. 5.4 (d) and has the name "set-point-on-I-only controller."

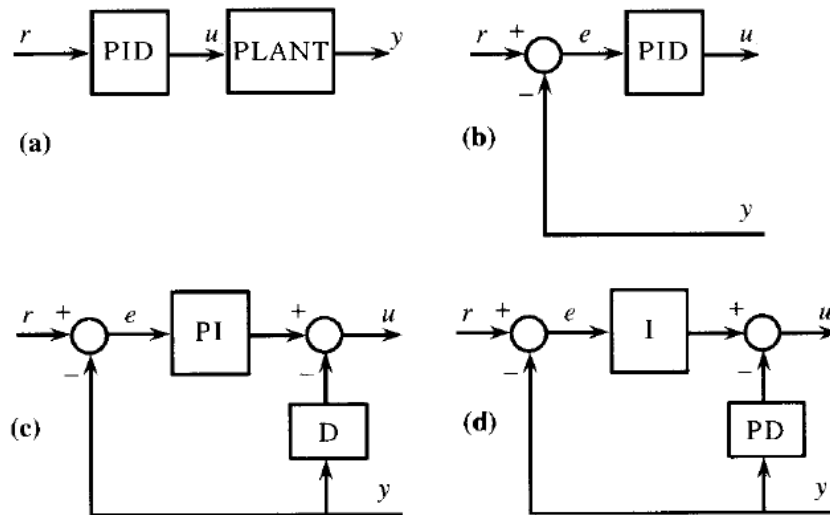


Figure 5.4 - PID Controller configurations: (a) Open loop, (b) textbook PID, (c) derivative-of-output, and (d) set-point-on-I controller.

For the MRB system, a feedback is introduced to calculate the error between the outputted slip ratio, s_r , and the constant continuous reference slip ratio, s_{rd} , and pass it as an input to the controller. Thus, the textbook PID controller is utilized. The resulting system drawn on SIMULINK with the built-in PID block is shown in Figure 5.5. It should be noted that (anti-windup) was enabled in the PID block to avoid time response delays because the input electric current is bounded between 0 and 2 *Amps*.

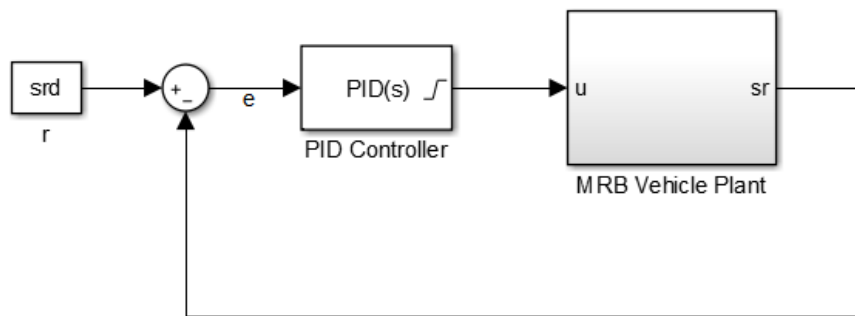


Figure 5.5 - PID Controller connection to the MRB Vehicle Plant.

4.3.3. PID Controller Design:

The conventional control law of the textbook PID controller is described as:

$$u(t) = i = k_P e(t) + k_I \int e(t) + k_D \frac{d}{dt} e(t) \quad (92)$$

where k_P , k_I and k_D are simply proportional, integral and differential gains, respectively and $e(t)$ is the error signal. In the Laplace domain, which is utilized by the PID block on SIMULINK, the control law becomes:

$$U(s) = \left(k_P + k_I \frac{1}{s} + k_D \frac{N}{1 + N \frac{1}{s}} \right) E(s) \quad (93)$$

where N is called the taming factor, usually varied between 3 and 10 [34]. Its purpose is to limit the amplification of high-frequency gains and makes the controller easier to build.

The slip ratio output from the MRB plant is subtracted from the referenced desired slip ratio to create an error signal, $e(t)$. Figure 5.2 shows that despite the surface conditions of the road, the optimal slip ratio is always near 0.2. Thus, the input of the system is the constant desired value of 0.2, which yields an error signal: $e(t) = 0.2 - s_r$.

The error value between the two numbers is then considered as input into the designed PID controller, which would predict the amount of electric current the dynamic MRB model needs to remain close to the desired slip ratio (to reduce the inputted error). The estimated value of current is to then be fed into the MRB-vehicle plant.

The design of the nonlinear closed-loop feedback MRB system with PID controller is carried out by the trial and error in the following order. First, the parameters k_I and k_D are set to 0 while several values for the gain k_P are investigated. The system acts as if it had proportional controller only. The effect of the tested gains on slip ratio is tracked to find the best fit. As seen in Fig. 5.6, after 7 trials, the best fit which yielded the least initial overshoot was found to be $k_P = 29$.

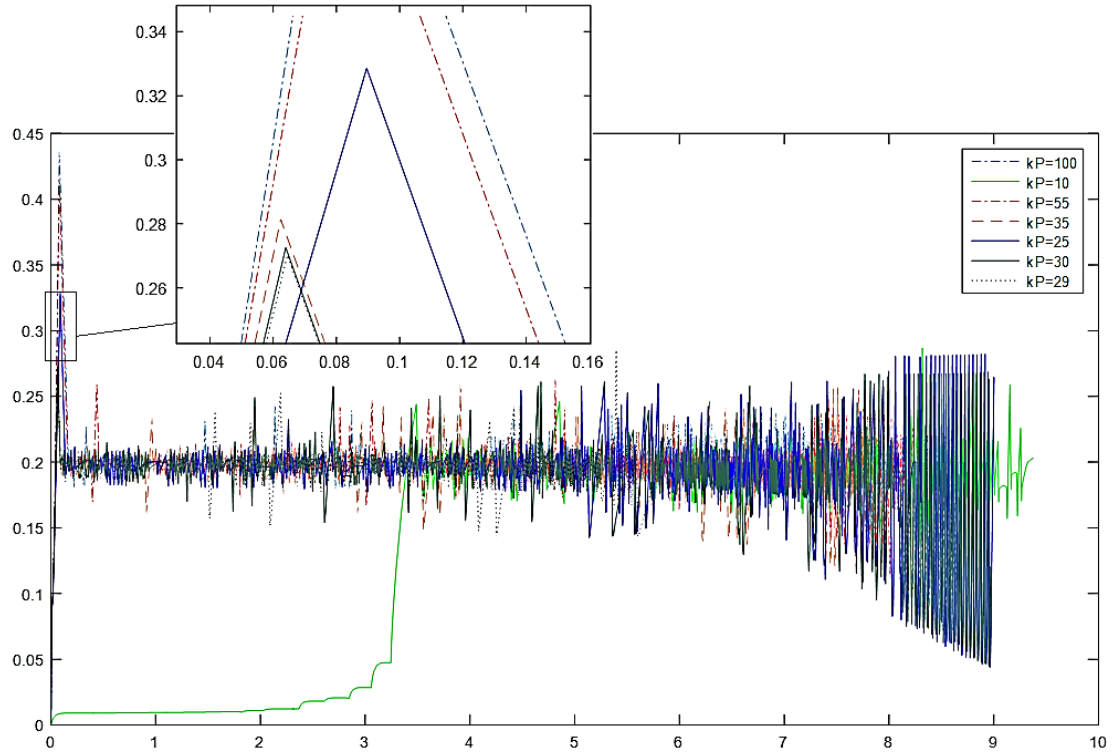


Figure 5.6 - Slip ratio with PID controller for varied proportional gains, k_P , $k_I=k_D=0$.

Next, with proportional gain fixed at $k_P=29$, different values are given to the integral gain k_I and the resulting slip ratio is monitored. Figure 5.6 shows that a small change in the gain k_I can amplify the overshoot. Several trails with smaller values were tested and the gain of -0.1 was chosen.

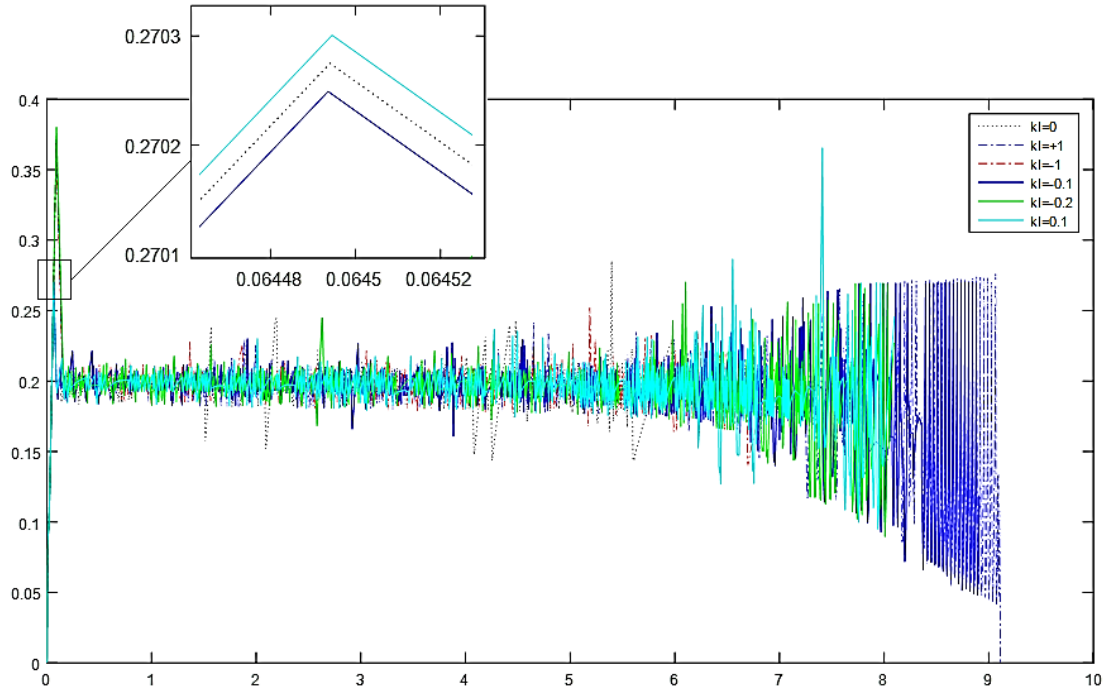


Figure 5.7 - Slip ratio with the PID controller for varied integral gains, k_I , $k_p=29$ and $k_D=0$.

The same trial and error procedure is performed to determine the derivative gain, k_D , while fixing the proportional and integral gains at 29 and -0.1 values, respectively. The tested values and their effect on the slip ratio are shown in Fig. 5.8. The selected value for derivative gain was found to be $k_D = 0.3$.

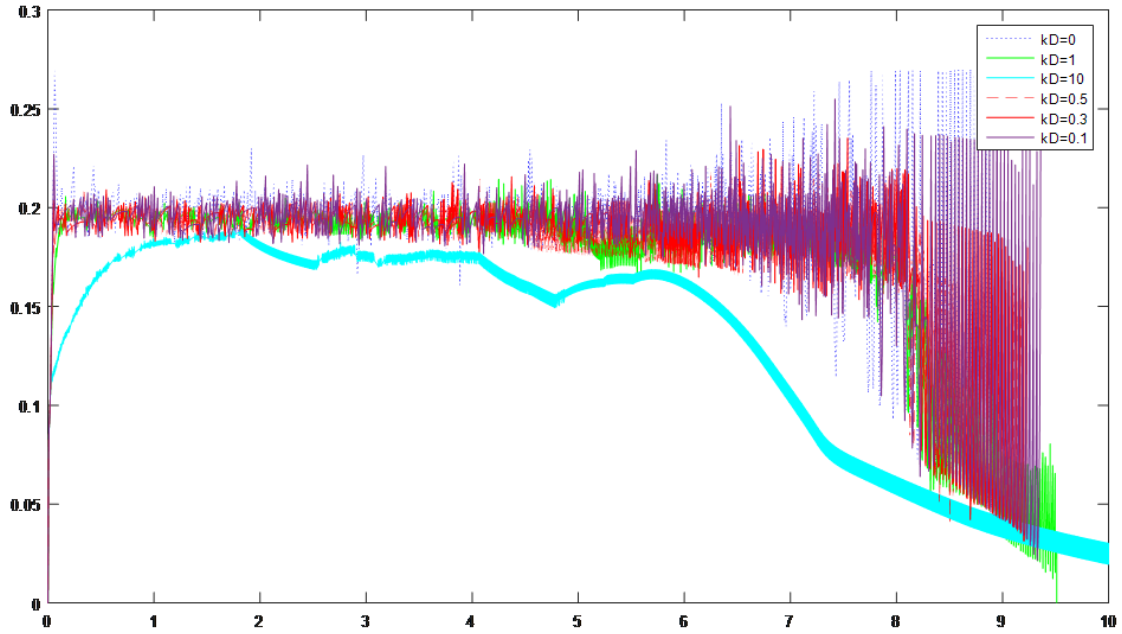


Figure 5.8 - Slip ratio with the PID controller for varied proportional gains, k_D , $k_p=29$ and $k_i=-0.1$.

5.4. Simulation Results:

5.4.1. Effect of the Time Constant block:

The first aim of simulation results is to record the effect of the inductive time constant on the brake performance. The simulation is run twice: One with the inputted current passed through the TC block and another with the output of the PID controller directly supplied to the torque generating code. The simulation was performed on a dry asphalt road condition. The resulting vehicle and wheel speeds, torque generation, slip ratio, and electric current estimated by the controller for both simulation runs are shown in Figure 5.9.

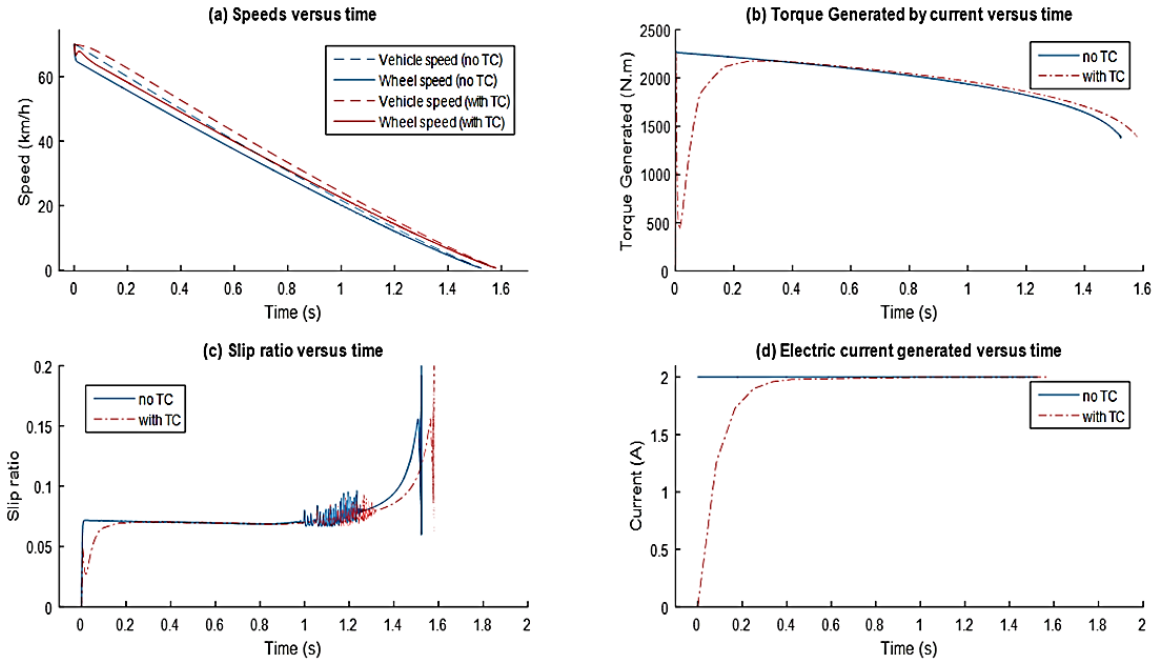


Figure 5.9 - Simulation Results with and without TC response.

Figure 5.9 (a) shows a slight increase of 0.1 seconds in the vehicle stopping time. This can be explained by the response delay effect on the generated braking torque. The blue line of Fig. 5.9 (b) represents the required braking torque to optimal performance while the dotted red line represents the actual braking torque achieved by the MRB. The slip ratio shows a smoother start with TC which results in a similar signal delayed by 0.1 seconds. The effect of the TC can be perfectly illustrated in Fig. 5.9 (d) where the blue line represents the applied electric current and the red dotted line characterizes the effective electric current present in the MRB's electromagnet.

5.4.2. Simulation results on different road conditions:

Additional case studies on how the system reacts on wet, snowy and icy roads are performed. The resulting variations of speed, torque, slip ratio and applied current as a function of time are shown in Figures 5.10, 5.11 and 5.12, for wet, snowy and icy roads, respectively.

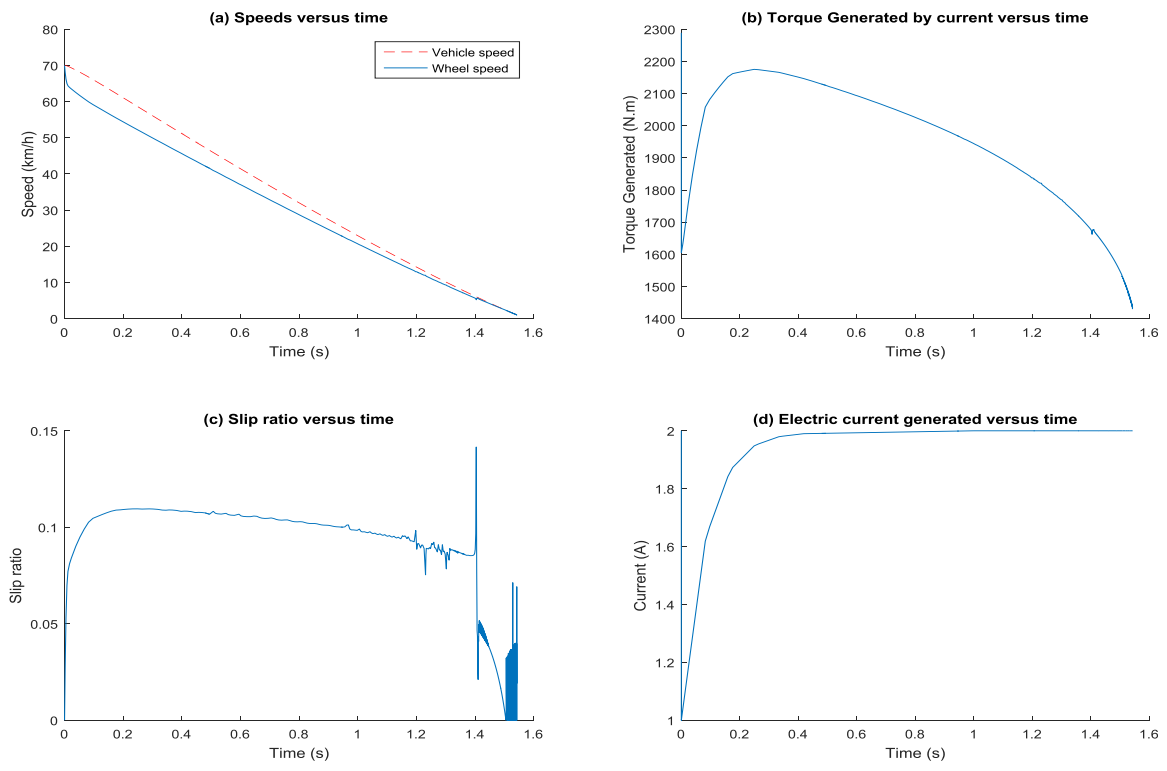


Figure 5.10 - Simulation results for wet roads.

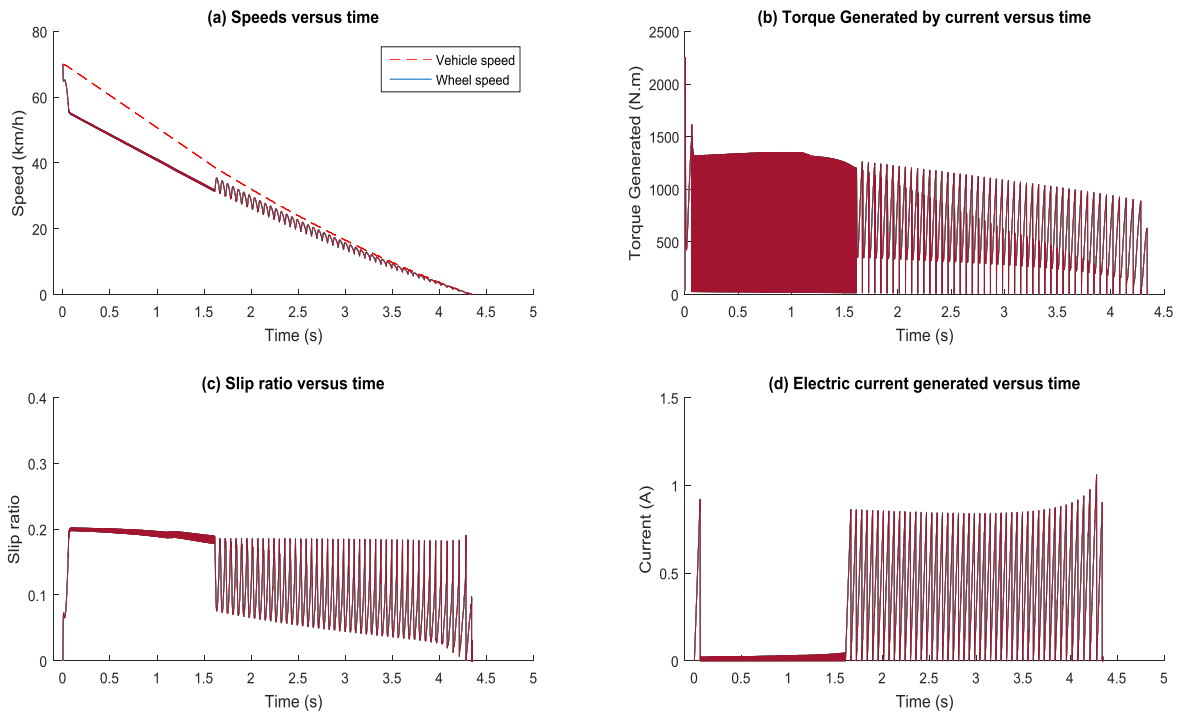


Figure 5.11 - Simulation results for a snowy road.

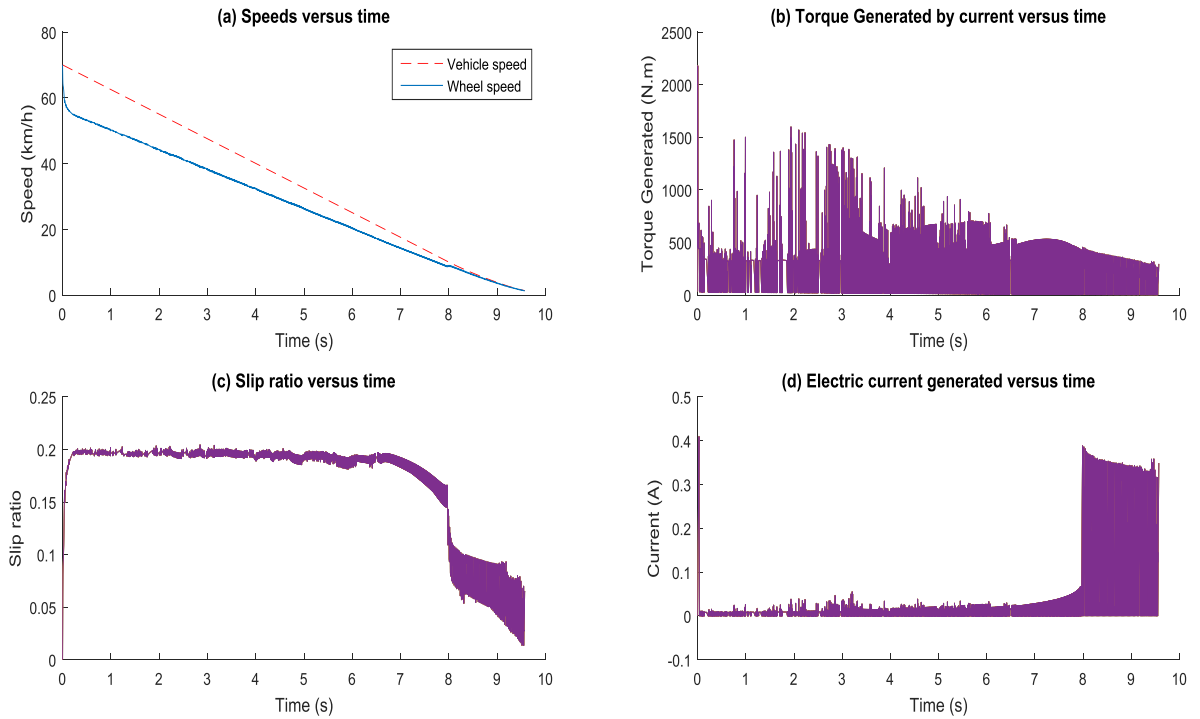


Figure 5.12 - Simulation results for an icy road.

The first thing to notice in the simulation results shown in above figures is that the vehicle speed is decreasing in a linear manner for all road conditions. The stopping time for both dry and wet roads is less than 1.6 seconds from a 70 *km/hr* cruise. The estimated torque required for dry roads is the maximum braking torque capacity of the MRB. The torque produced at 2A current input is seen in Fig. 5.10 (b). The only different between the results of the two road conditions, dry and wet, is the value of slip ratio. Since the vehicle driving on a wet road has a higher tendency to slide, the value of the slip ratio at the same braking torque value is higher for wet roads than it is on dry roads. Figure 5.9 (c) shows that the slip ratio on a dry road is around 0.07 while for that of wet road, Fig. 5.10 (c), it reached to higher values of nearly 0.11.

In the case of a snowy road, however, the generated torque is quickly controlled at the value of around $1,300 \text{ Nm}$ as it gets close to the slip ratio limit of 0.2. The supplied electric current instantly decreased from 0.9 A to nearly 0.1 A to supply the sufficient torque to allow smooth control of the wheel speed. After nearly 1.5 seconds, some fluctuations are seen as the wheel speed is decreasing. The brake exhibits a similar behavior to a conventional Anti-lock Braking System (ABS) but with much faster response and with fewer fluctuations. Overall, its effect on the vehicle is negligible as the vehicle speed was efficiently brought down to zero in under 4.5 seconds. These results can be seen in Fig. 5.11.

Finally, controlling the braking torque produced by the MRB on icy roads seemed most challenging due to its very low coefficient of friction. Nonetheless, the controlled system succeeded to limit the slip ratio at around 0.2 for up to 70% of the braking time, stopping the vehicle at less than 10 seconds. With the highly fluctuating torque, the effective electric current within the MRB remained under 0.1 A for nearly 80% of the total braking time, only increasing to 0.4 A at the final 2 seconds of braking.

Comparing the obtained results with the results of Park et al. [5], the stopping time reported using sliding mode controller for dry and icy roads were 2.5 and 15 seconds, respectively. Despite the simulation of the time response effect, the proposed design of this research achieved an impressive 36% increase in braking efficiency in terms of stopping time.

5.4.3. Open-loop response of the MRB-Vehicle plant:

A simulation test is run on the MRB-Vehicle plant to evaluate its open loop response – i.e. the response of the brake without the controller. The inputted electric current is supplied at a constant value. For dry and wet asphalt roads, the maximum torque is not sufficient to lock the

wheels and cause sliding. Thus, the open loop response of the brake for these two road conditions is the exact same with and without the controller. Nonetheless, wheel lockup can be quickly reached at lower torque values when the vehicle is driving on a snowy road and even less on an icy road. The response of the brake system on an icy road is recorded for different applied current values and the results are presented in Fig. 5.13. It is shown that that the wheel would lock up for values of electric current as low as $0.3A$. With that input, the wheel lock-up is seen within 0.55 seconds. For the input of $0.5A$, wheel lock-up occurs after 0.15 seconds of braking - that is even before the equivalent current in the MRB reaches $0.4A$ (See Fig. 5.13(d) at $0.5A$). It should be noted that wheel lock-up does not take place at a current of $0.2A$ or less.

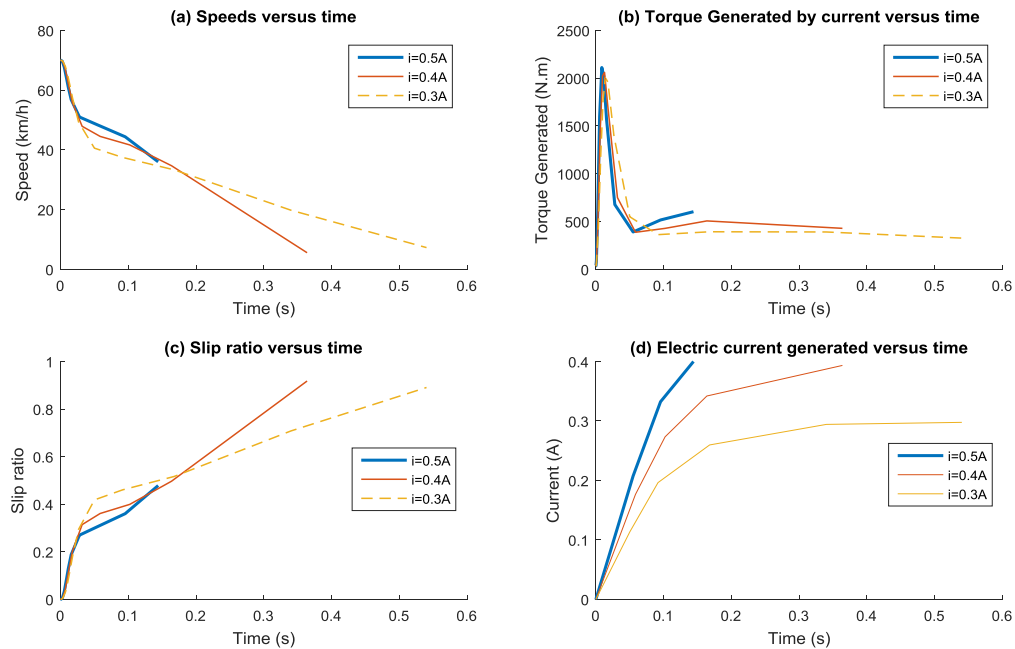


Figure 5.13 - Open loop system responses due to constant current inputs-Icy Road.

5.4.4. Antilock-Braking-System of the conventional hydraulic brake:

MATLAB's built in Anti-Lock Braking System (ABS) that models the behavior of a vehicle model with hydraulic brakes is utilized to compare with the obtained results for the novel MRB design. The SIMULINK model can be opened by running the MATLAB command "sldemo_absbrake" in the command window. The same vehicle model parameters are used and starting from the same initial velocity, the simulation results for the four different road conditions are plotted below.

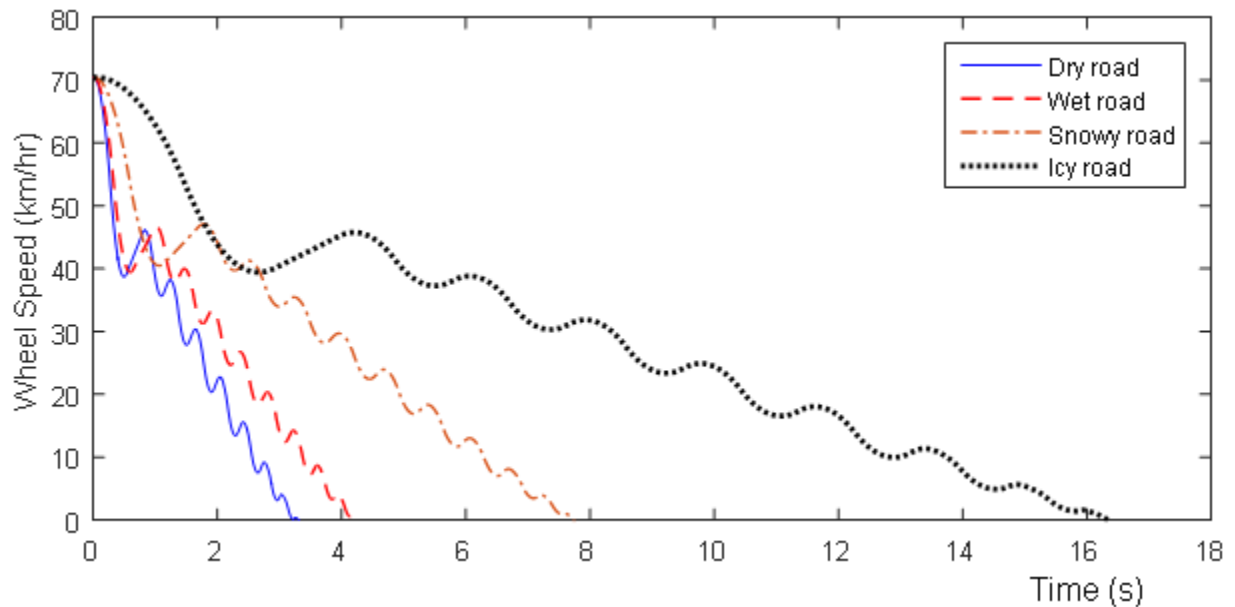


Figure 5.14 - Wheel speed of a hydraulic brake with ABS for different road conditions.

It can be seen from Fig. 5.14 that the anti-lock braking system of the conventional hydraulic brake (CHB) exhibits a sinusoidal decay for wheel speed. This is due to the response delay of the CHB. The proposed MRB design displays a smoother decrease in wheel speed due to its faster response time and more accurate controllability. The vehicle stopping time is slightly over 3 seconds on a dry road, 4 seconds on a wet road, approximately 8 seconds on a snowy road and a

bit over 16 seconds for an icy road. These numbers are significantly reduced by the proposed MRB design.

5.5. Summary:

In this chapter, a quarter vehicle model is presented to examine the real-vehicle performance of the proposed MRB design. Case studies have been done to evaluate the performance of the controlled MRB on dry, wet, snowy, and icy road conditions. To control and regulate the slip ratio, a PID controller is designed and integrated with the MRB vehicle model. The PID controller proved to significantly improve the brake's anti-lock properties. Comparing the results in Fig. 5.14 to the results of the proposed design, the proposed MRB is able to stop a car in 50% less time on a dry road, around 60% on a wet road, and nearly 42% on snowy and icy roads. In conclusion, the proposed MRB design of this research is at least 42% more efficient than the conventional hydraulic braking system. Moreover, it has been shown that the proposed MRB design in this study is 36% more efficient than the previous conventional MRB designs.

CHAPTER 6

CONCLUSIONS

6.1. Introduction:

The main aim of this research thesis is to fundamentally study Magnetorheological Brake (MRB) and to develop a formal multidisciplinary design optimization formulation to improve its performances. Despite the fact that there were several attempts by researchers around the world to design a suitable MRB for application in the automotive industry, all these designs were classified as insufficient and unacceptable mainly due to the performance of MRB in the off-state. In this research, a novel MRB design with zero off-state viscous torque has been introduced, numerically tested, and proved to be capable of being implemented in real vehicle applications. The torque equations were derived based on Bingham and Herschel-Buckley mathematical models. Magnetostatic analysis has been conducted to find the approximate relation between the induced magnetic field in the MR gap and the applied current and electromagnet geometrical parameters. This has been further validated using the developed magnetic finite element model. Steady state heat analysis has also been performed to evaluate the temperature build up in the MR fluid. This is followed by the formulation of a formal multi-objective design optimization problems to identify the optimal parameters of the conventional and proposed MRB designs for different configurations. Genetic Algorithm (GA) and combined GA and Sequential Quadratic Programming (SQP) techniques have been utilized to solve the optimization problems and results are compared. Finally, the functionality of the proposed optimal MRB design has been tested in a quarter vehicle model. The close loop performance has been evaluated using a PID controller. The resulting novel MRB design proved to be capable of reducing the braking distance and time while providing a smoother and more comfortable deceleration.

6.2. Major Contributions:

The major contributions of this research to the literature are listed as follows:

- Propose an innovative MRB model for real-vehicle applications that completely de-couples the brake's working modes leaving no energy loss.
- Develop torque equations to accurately model the conventional and the proposed MRB designs for single and multiple disk configurations.
- Formulate and validate an analytical model to represent the magnetic circuit of MRB and obtain a mathematical representation of the relationship between magnetic flux intensity and applied electric current.
- Perform heat transfer analysis to investigate the maximum reachable temperature of the MRB.
- Define an objective function based on different design specifications and perform several optimization approaches under multidisciplinary constraints to reach the best possible configuration for an automotive MRB.
- Improvement on the electric circuit of the MRB to enhance its response time by the addition of a resistor in series.
- Investigation on the closed loop performance of the proposed MRB in a quarter vehicle model using PID controller to control the sliding of the vehicle on different road conditions.

6.3. Explanation of Limitations:

The present research project has mainly focused on investigating and improving the theoretical design and does not address the actual manufacturing plan and implementation procedure which is the subject of future investigation.

For the control model in Chapter 5, it is assumed that the surface the vehicle is moving on is a straight asphalt surface. The result would not be the same for other surfaces conditions such as inclines or declines. Furthermore, other factors like surface disturbances (bumps, holes...) and tire pressure are related to the problem but not addressed.

Additional limitations are the material selection process. A more thorough exploration of material selection would have further improved the performance of the MRB. Finally, no details were given on the application of O-ring sealing.

Furthermore, some assumptions have been made to ease calculations and simplify some problems. In the magnetic circuit analysis of the MRB, the ratio of relative permeability of the MR fluid and steel is assumed to be constant when in reality they are varied and highly dependent on external conditions like temperature changes. Additionally, while performing the heat analysis, the active MR fluid is modeled as a solid body that exerts a constant pressure equal to the shear stress on its surrounding contact surfaces. Finally, the proposed novel design includes the assumption of perfect transition between the on and off state. The delay of this transition is considered constant and added to the brake's response time due to electric current saturation. More elaboration on this transition can be achieved through formulating a Multiphysics problem that can simultaneously model the magnetic, fluid flow, structural and heat analysis. This is also a subject of future investigation.

6.4. Recommendations for Future Works:

While the present research work has significantly advanced the state of the art in MRB design, there are still some interesting future works which can pave the way for practical implementation of these emerging technologies. These are summarized as follows:

- 1- Fabrication and testing of the proposed novel MRB design to realize its effectiveness experimentally.
- 2- Development of an accurate Multiphysics problem that can simultaneously model the magnetic, fluid flow, structural and heat analysis.
- 3- Improving the performance of the existing proposed MRB design. This can be achieved by fine-tuning some of the design variables. For example, performing structural analysis to minimize the weight of the core of the rotor. Also, further investigation on the PM through simulating the distribution of fluxes in the shear gap region and designing each PM separately based on the flux in each region.
- 4- Thorough investigation in the vehicle application of the MRB. For instance, study on the effect of cyclic braking, the true power of the car battery based on its type, rating and energy storing ability.
- 5- Development of other control strategies for the MRB-Vehicle system. More investigation on the development of appropriate controllers are required to improve the traction control, vehicle ride and stirring comfort. Finally, the MRB operates poorly at low speeds.
- 6- Investigation on hybrid braking system integrating both MRBs and CHBs. As an example, the two front wheels could be equipped with CHBs while the two rear wheels are equipped with MRBs. Such system requires less power and is expected to provide a more effective braking with good controllability for the ride, braking and steering.

REFERENCES

- [1] A. Mohammad, C. Yao X. L. and J. Deng, "Review of Magnetorheological (MR) fluids and its applications in vibration control," *J. Mar. Sci. Appl.*, vol. 5, p. 17, 2006.
- [2] P. Blau and H. I. Meyer, "Characteristics of wear particles produced during friction tests of conventional and unconventional disc brake materials," *Wear*, pp. 1261-1269, 2003.
- [3] J. Wahlström, "A study of airborne wear particles from automotive disc brakes," Ph.D. thesis, Royal Institute of Technology, Sweden, 2011.
- [4] M. T. Avraam, "MR-fluid brake design and its application to a portable muscular rehabilitation device," Ph.D. thesis, Université Libre de Bruxelles, Bruxelles, Belgium, 2009.
- [5] E. Park, D. Stoikov, L. Falcao de Luz and A. Suleman, "A performance evaluation of an automotive magnetorheological brake design with a sliding mode controller," *Mechatronics*, vol. 16, no. 16, p. 405, 2006.
- [6] E. J. Park, L. Falcao da Luz and A. Suleman, "Multidisciplinary design optimization of an automotive magnetorheological brake design," *Computer and Structures*, vol. 86, p. 207, 2007.
- [7] Y. Shiao and Q. A. Nguyen, "Structural Analysis and Validation of the Multi-pole Magnetorheological Brake for Motorcycles," *Procedia Engineering*, vol. 76, p. 24, 2014.
- [8] d. Gmbh, "Braking at its best," [Retrieved Online on October 08, 2015]. Available: www.dSPACE.com.
- [9] J. Krantz, "System and method for removing brake dust and other pollutants". Patent Patent application US 13/109,891, 2011.
- [10] D. J. Carlson, "Magnetorheological brake with integrated flywheel". United States Patent Office Patent US Patent 6,186,290 B1, 2001.
- [11] G. M. Webb, "Exercise Apparatus and Associated Method Including Rheological Fluid Brake". United States Patent Office Patent US Patent No. 5810696, 1998.
- [12] S. Bydon, "Construction and Operation of Magnetorheological Rotary Brake," *Archiwum Process Control*, p. 20, 2002.
- [13] B. Liu, W. H. Li, P. B. Kosasih and X. Z. Zhang, "Development of an MR brake based haptic device," *Smart Materials and Structures*, vol. 15, p. 1960, 2006.
- [14] C. M. Chew and G. S. Hong, "Development of a compact double-disk magnetorheological fluid brake," *Robotica*, vol. 25, p. 493, 2006.

- [15] W. Zhou, C. M. Chew and G. S. Hong, "Development of a compact double-disk magnetorheological fluid brake," *Robotica*, vol. 55, p. 493, 2006.
- [16] K. Karakoc, E. J. Park and A. Suleman, "Design considerations for an automotive magnetorheological brake," *Mechatronics*, vol. 18, no. 8, p. 434, 2008.
- [17] Q. Nguyen and S. Choi, "Optimal design of an automotive magnetorheological brake considering geometric dimensions and zero-field friction heat," *Smart Mater. Struct.*, vol. 19, 2010.
- [18] J. D. Carlson, "What makes a good MR fluid?," *J. Intell. Mater. Syst. Struct.*, vol. 13, p. 431, 2002.
- [19] P. B. Usoro, A. I. Smith, K. C-K, G. Moser and G. Sommer, "Magnetorheological fluid clutch". Patent US Patent Specification 6,318,531 B1, 2001.
- [20] D. Guth and J. Maas, "Magnetic fluid control". Patent DE Patent Specification 10 2011 119 919.9, 2011.
- [21] D. Guth, M. Schamoni and J. Maas, "Magnetic fluid control for viscous loss reduction of high-speed MRF brakes and clutches with well-defined fail-safe behavior," *Smart Mater. Struct.*, vol. 22, p. 094010, 2013.
- [22] I. Arief and P. Mukhopadhyay, "Synthesis of dimorphic MR fluid containing NiCo nanoflowers by the polymer assisted polyol method and study of its magnetorheological properties," *Physica B*, vol. 448, p. 73, 2014.
- [23] *MR Brake Product Bulletin MRB-2107-3*, Cary, NC: Division, Lord Corporation Material, 2003.
- [24] M. Zubieta, S. Eceolaza, M. J. Elejabarrieta and M. M. Bou-Ali, "Magnetorheological fluids: characterization and modeling of magnetization," *Smart Mater. Struct.*, vol. 18, p. 095019, 2009.
- [25] B. Assadsangabiej, F. Daneshmand, F. Vahdati, M. Eghtesa and Y. Bazargan-laria, "Optimization and Design of disk-type MR brakes," *Intl. J. Auto. Tech.*, vol. 12, p. 921, 2011.
- [26] Supermagnete, "How do you calculate the magnetic flux density?," [Retrieved Online on June 11, 2016]. Available:
<https://www.supermagnete.de/eng/faq/How-do-you-calculate-the-magnetic-flux-density#ring-magnet>.
- [27] Supermagnete, "Physical Magnet Data," [Retrieved Online on June 12, 2015]. Available:
https://www.supermagnete.de/eng/data_table.php.

- [28] D. Majcherczak, P. Dufrenoy and M. Nait-Abdelaziz, "Third Body Influence on Thermal Friction Contact Problems: Application to Braking," *Journal of Tribology*, vol. 127, p. 89, 2005.
- [29] F. Talati and S. Jalalifar, "Analysis of heat conduction in a disk brake system," *Heat Mass Transfer*, vol. 45, p. 1045, 2009.
- [30] C. Rossa, A. Jaegy, J. Lozada and A. Micaelli, "Design Considerations for Magnetorheological Brakes," in *IEEE ASME Transactions on Mechatronics*, 2014.
- [31] T. Gillespie, *Fundamentals of vehicle dynamics.*, Soc Automot Engrs, 1992.
- [32] L. Falcaõ da Luz, "Design of a magnetorheological brake system.," M.A.Sc. thesis, University of Victoria, Victoria, BC, Canada, 2004.
- [33] A. B. Will , S. Hui and S. Zak, "Sliding mode wheel slip controller for an antilock braking system," *Int. J. of Vehicle Design*, vol. 19, no. 6, p. 523, 1998.
- [34] C.-T. Chen, *Analog and Digital Control System Design: Transfer-Function, State-Space, and Algebraic Methods*, Oxford University Press; 1 edition , 2006.
- [35] "Magneto-Rheological (MR) Fluid," LORD Corporation, [Retrieved Online on September 20, 2015]. Available: <http://www.lord.com/products-and-solutions/active-vibration-control/industrial-suspension-systems/magneto-rheological-%28mr%29-fluid>.
- [36] F. P. INCROPERA, D. P. DEWITT, T. L. BERGMAN and A. S. LAVINE, *Fundamentals of Heat and Mass Transfer - 6th ed.*, JOHN WILEY & SONS, 2007.
- [37] E. Slotine and L. Weiping, *Applied nonlinear control*, Englewood Cliffs, NJ: Prentice-Hall, 1991.
- [38] X. Wang and F. Gordaninejad, "Study of field-controllable, electro- and magneto-rheological fluid dampers in flow mode using Herschel–Bulkely theory," in *Proceedings of SPIE smart structures and materials conference*, Newport Beach, CA, 2000.

APPENDIX A: MRB WEIGHT ESTIMATION EQUATION

A.1. The conventional MRB Design:

To estimate the weight of the 2-disk MRB, first the volume of each part is calculated from its geometric dimensions. For the rotary discs, the volume can be described as:

$$V_d = 2\pi[R_0^2 - R_1^2]b_d \quad (A1)$$

The non-magnetic shaft that connects the MRB to the main wheel axle of a vehicle is of inner radius, R_b , equated to 70% of the outer radius outer radius, R_l . The brake's shaft consists of a plane of thickness b_s and openings that allow the brake to be installed on the bolts of the wheel shaft. The combined volume of the Aluminum shaft and core, ignoring the bolt orifices, are:

$$V_{al} = \pi\left\{(R_1^2 - R_b^2)L + R_b^2b_s + (L - 2b_h)\left[(R_0 + d_0 + c)^2 - (R_0 + d_0)^2\right]\right\} \quad (A2)$$

As for the outer casing of the MRB, the volume is calculated as:

$$V_c = 2\pi b_h\left[(R - t)^2 - R_1^2\right] + \pi L\left[R^2 - (R - t)^2\right] + \pi b_c\left[(R_0 + d_0)^2 - (R_1 + d_i)^2\right] \quad (A3)$$

Finally, the volume of the gap of the MRB where the fluid lies is:

$$V_f = \pi\left[2(d + d_c)(R_0^2 - R_1^2) + 2(b_d + d + d_c)\left((R_0 + d_0)^2 - R_0^2\right) + b_c\left((R_1 + d_i)^2 - R_1^2\right)\right] \quad (A4)$$

The volume of the copper AWG21 wires can be found as:

$$V_w = 2\pi\left(R_0 + d_0 + c + \frac{h_c}{2}\right)\left(N_c \frac{\pi d_w^2}{4}\right) \quad (A6)$$

The final equation for the weight of the MRB can now be represented by:

$$W_{MRB} = \rho_d V_d + \rho_{al} V_{al} + \rho_c V_c + \rho_f V_f + \rho_w V_w \quad (A7)$$

where ρ_m , ρ_{al} , ρ_c , ρ_f , and ρ_w are the densities of the materials used for the steel disk, aluminum shaft and core, the steel casing, the MR fluid and copper wire, respectively.

A.2. Novel MRB Design:

Similarly, the volumes of the parts of the novel design are defined. The rotary discs are composed of two parts of different material types, the volumes of the magnetic and nonmagnetic components can be described as:

$$V_{dm} = 2\pi \left[R_0^2 - (R_2 - d_f)^2 \right] b_d \quad (\text{A8})$$

$$V_{dal} = 2\pi \left[(R_2 - d_f)^2 - R_1^2 \right] b_d \quad (\text{A9})$$

The shaft and core volumes are the same as that of the conventional design, V_{al} , in Eq. (A.2). The outer casing of the novel MRB design is a composite of metal and aluminum. The volumes of the two components are calculated as:

$$V_{cm} = 2\pi b_h \left[(R - t)^2 - R_2^2 \right] + \pi L \left[R^2 - (R - t)^2 \right] + \pi b_c \left[(R_0 + d_0)^2 - R_2^2 \right] \quad (\text{A10})$$

$$V_{cal} = \pi (b_c + 2b_h - 4D_m) \left[R_2^2 - (R_1 + d_i)^2 \right] + \pi (b_c + 2b_h) \left[(R_2 - g_a - d_f - L_m)^2 - (R_1 + d_i)^2 \right] \quad (\text{A11})$$

The volume of the MR fluid is:

$$V_{fs} = 2(d + d_c) \pi (R_0^2 - R_2^2) \quad (\text{A12})$$

Finally, the volume of the permanent magnets is:

$$V_{PM} = D_m L_m (\pi R_e^2) \quad (\text{A13})$$

The total weight of the novel MRB design can be estimated as:

$$W_{MRB_n} = \rho_m (V_{dm} + V_{cm}) + \rho_{al} (V_{al} + V_{dal} + V_{cal}) + \rho_f V_{fs} + \rho_{PM} V_{PM} + \rho_w V_w \quad (\text{A14})$$

where ρ_{PM} is the density of the Permanent Magnet.

APPENDIX B: CATIA DRAWING OF THE NOVEL MRB

The following page contains the schematic drawing of the final novel MRB model. The isometric view and inner (inner side of the vehicle) view are drawn with a 1:8 scale. The outer view, bottom view, a section view (C-C), and a section cut (A-A) are drawn with a scale of 1:4. A zoomed in detailed view (Detail B) presents the major components of the proposed MRB design in its actual scale. The main dimensions are shown.

